Simulations of COMPASS Vertical Displacement Events with a self-consistent model for halo currents including neutrals and sheath boundary conditions

F.J. Artola[1], A. Loarte[1], E. Matveeva[5,6], J. Havlicek[6], T. Markovic[6], J. Adamek[6], J. Cavalier[6], L. Kripner[6], G.T.A. Huijsmans[3,4], M. Lehnen[1], M. Hoelzl[2], R. Panek[6], the COMPASS team[6], and the JOREK team[7]

[1] *ITER Organization, Route de Vinon sur Verdon, 13067 St Paul Lez Durance Cedex, France*
[2] *Max Planck Institute for Plasmaphysics, Boltzmannstr. 2, 85748 Garching, Germany*
[3] *CEA, IRFM, F-13108 St. Paul-lez-Durance cedex, France*
[4] *Eindhoven University of Technology, 5612 AP Eindhoven, The Netherlands*
[5] *Charles University, Faculty of Mathematics and Physics, Prague, Czech Republic*
[6] *Institute of Plasma Physics of CAS, Za Slovankou 3, 182 00 Prague, Czech Republic*
[7] *please refer to [M Hoelzl, G T A Huijsmans, S J P Pamela, M Becoulet, E Nardon, F J Artola, B Nkonga et al, Nuclear Fusion, in preparation]*

Corresponding author: **A. Loarte** Email: alberto.loarte@iter.org

Abstract

The understanding of the halo current properties during disruptions is key to design and operate large scale tokamaks in view of the large thermal and electromagnetic loads that they entail. For the first time, we present a fully self-consistent model for halo current simulations including neutral particles and sheath boundary conditions. The model is used to simulate Vertical Displacement Events (VDEs) occurring in the COMPASS tokamak. Recent COMPASS experiments have shown that the parallel halo current density at the plasma-wall interface is limited by the ion saturation current during VDE-induced disruptions. We show that usual MHD boundary conditions can lead to the violation of this physical limit and we implement this current density limitation through a boundary condition for the electrostatic potential. Sheath boundary conditions for the density, the heat flux, the parallel velocity and a realistic parameter choice (e.g. Spitzer's resistivity and Spitzer-Härm parallel thermal conductivity) extend present VDE simulations beyond the state of the art. Experimental measurements of the current density, temperature and heat flux profiles at the COMPASS divertor are compared with the results obtained from axisymmetric simulations. Since the ion saturation current density (J_{sat}) is shown to be essential to determine the halo current profile, parametric scans are performed to study its dependence on different quantities such as the plasma resistivity and the particle and heat diffusion coefficients. In this respect, the plasma resistivity in the halo region broadens significantly the J_{sat} profile, increasing the halo width at a similar total halo current.

1 Introduction

The operation of large scale tokamaks such as ITER and DEMO requires a Disruption Mitigation System (DMS) to minimize the impact of disruption loads on the plasma facing components and on the vacuum vessel [19]. The design and optimization of such a system must be guided by experiments and validated numerical codes. In order to quantify the load reduction provided by the different disruption mitigation schemes, high fidelity simulations should be able to predict the worst case scenarios in terms of heat and electromagnetic loads.

During disruptions, currents flowing along the open field lines (halo currents) can produce large forces on the vacuum vessel and also large heat loads on the plasma facing components by

converting the plasma magnetic energy into thermal energy via Ohmic heating. The parametric dependencies of the current density and the heat flux profiles during disruptions are not yet well understood. MHD simulations for disruptions are numerically challenging and therefore previous simulations have typically oversimplified the boundary conditions for different plasma quantities (e.g. Dirichlet conditions for temperature and density).

In this paper we present, for the first time, a fully self-consistent model for halo current simulations including neutral particles and a set of advanced boundary conditions. Sheath boundary conditions for the density, the heat flux and the parallel velocity together with a realistic parameter choice (e.g. Spitzer's resistivity η and Spitzer-Härm parallel thermal conductivity $\kappa_\parallel$) extend non-linear MHD VDE simulations beyond the state of the art. Additionally we introduce a boundary condition for the electrostatic potential in order to limit the halo current density to the ion saturation current. This limitation comes from basic sheath plasma physics and has recently been observed in COMPASS disruption experiments [1]. Neutral particles are required to calculate the evolution of the boundary density, which is key to determine the ion saturation current density. As a first step, the neutral particle density is modeled with a fluid continuity equation and an effective diffusion coefficient. For this work we use the JOREK code [15, 11] to perform axisymmetric MHD simulations of COMPASS VDEs and compare the modeled results with experimental measurements. Since the ion saturation current density (J_{sat}) will be shown to be essential to determine the halo current profile, parametric scans are performed to study its dependence on different quantities such as the plasma resistivity and the particle and heat diffusion coefficients. Recent simulations with the NIMROD code [8] have explored the effect of different boundary conditions for the plasma density, temperature and velocity on VDEs [4]. However the important effects of neutral particles and the ion saturation current limitation were not included.

This paper is organized as follows: In section 2 the MHD model and the boundary conditions are explained in detail. The numerical setup is presented in section 3 together with the parameter choice used to simulate the COMPASS VDE experiments. The large effect of the sheath boundary conditions on the evolution of the halo current is discussed in 4. In that section, the influence of plasma viscosity, neutral particle reflection and the implemented minimum heat and particle fluxes are also discussed. The comparison of the simulations with the experimental results is given in section 5. The dependencies of the halo current profile on different parameters is researched in section 6. Finally the conclusions are summarized in section 7.

2 Model and boundary conditions

The implicit non-linear code JOREK solves the extended magneto-hydrodynamic (MHD) equations in realistic tokamak geometries including open field line regions [15, 11]. In JOREK the poloidal plane is discretized with quadrilateral bicubic Bezier elements using an isoparametric mapping [6]. Fourier harmonics are used to decompose the toroidal direction and for the time stepping typically the Crank-Nicholson or the BDF2 Gears scheme are used. The code contains a hierarchy of different MHD models with various extensions. The MHD model used for this work includes an equation for fluid neutral particles

$$\frac{\partial \mathbf{A}}{\partial t} = \mathbf{v} \times \mathbf{B} - \eta \mathbf{J} - \nabla \Phi, \tag{1}$$

$$\rho \frac{\partial \mathbf{v}}{\partial t} = -\rho \mathbf{v} \cdot \nabla \mathbf{v} - \nabla p + \mathbf{J} \times \mathbf{B} + \nabla \cdot \underline{\boldsymbol{\tau}} - (\rho \rho_n S_{ion} - \rho^2 \alpha_{rec}) \mathbf{v}, \tag{2}$$

$$\frac{\partial \rho}{\partial t} = -\nabla \cdot (\rho \, \mathbf{v}) + \nabla \cdot (\underline{\mathbf{D}} \nabla \rho) + (\rho \rho_n S_{ion} - \rho^2 \alpha_{rec}), \tag{3}$$

$$\frac{\partial \rho_n}{\partial t} = \nabla \cdot (\underline{\mathbf{D}}_n \nabla \rho_n) - (\rho \rho_n S_{ion} - \rho^2 \alpha_{rec}), \tag{4}$$

$$\frac{\partial p}{\partial t} = -\mathbf{v} \cdot \nabla p - \gamma p \nabla \cdot \mathbf{v} + \nabla \cdot (\underline{\boldsymbol{\kappa}} \nabla T) + (\gamma - 1) \eta J^2 - \xi_{ion} \rho \rho_n S_{ion} - \rho \rho_n L_{lines} - \rho^2 L_{brem} \tag{5}$$

with the following reduced MHD ansatz for the magnetic field ($\mathbf{B}$) and the mean plasma velocity ($\mathbf{v}$)

$$\mathbf{B} = \nabla \psi \times \nabla \phi + F_0 \nabla \phi, \tag{6}$$

$$\mathbf{v} = -\frac{R^2}{F_0} \nabla \Phi \times \nabla \phi + \mathbf{v}_\parallel, \tag{7}$$

where ψ is the poloidal magnetic flux and $F_0 = RB_\phi$ is a constant representing the main reduced MHD assumption, which is that the toroidal field is fixed in time. Note however that poloidal currents are not fixed in time and evolve according to the current conservation and momentum balance equations, but their contribution to the toroidal field is neglected due to the large vacuum field. A recent benchmark with full MHD codes has demonstrated that halo currents can be described accurately in this way [17]. The quantities shown in equations (1)-(7) are the magnetic potential ($\mathbf{A}$), the ion density (ρ), the neutral density (ρ_n), the total pressure (p), the total temperature ($T \equiv T_e + T_i$), the electrostatic potential (Φ) and the current density ($\mathbf{J}$). The parameters related to the neutral particle fluid are the ionization and recombination rates (S_{ion}, α_{rec}), the Deuterium ionization energy (ξ_{ion}) and the line (L_{lines}) and bremsstrahlung (L_{brem}) radiation coefficients. However the charge exchange process is not included, which leads to momentum losses at low temperatures ($T \sim 1-10$ eV) and will be included in future works. Other parameters in equations (1)-(7) are the plasma resistivity (η), the stress tensor($\underline{\boldsymbol{\tau}}$), the thermal conductivity and the particle diffusion coefficients ($\underline{\boldsymbol{\kappa}}, \underline{\mathbf{D}}, \underline{\mathbf{D}}_n$) and the ratio of specific heats (γ). The thermal conductivity coefficients $\underline{\boldsymbol{\kappa}}$ present a high anisotropy (i.e. $\kappa_\parallel \gg \kappa_\perp$) while the particle diffusion coefficients are normally isotropic. Note that the reduction of the equations is ansatz-based, conserves energy [7] and does not result from geometrical ordering assumptions. The effect of impurity radiation plays an important role in the disruption dynamics, however this effect is not included in the present simulations and it is left for future work.

The resistive wall and the free-boundary conditions are included by coupling JOREK to the STARWALL code [21, 12, 3]. The coupling is performed by solving the full vacuum domain with a Green's function method and therefore the vacuum does not need to be meshed. STARWALL uses the thin wall assumption and discretises the wall with linear triangular elements. Although the employed wall formalism is implemented for 3D thin walls including holes, the setup used here is restricted to an axisymmetric wall.

Boundary conditions

In this subsection, the boundary conditions used throughout this paper are explained. The free-boundary conditions for the poloidal magnetic flux are explained in detail in the references [12, 3].

Parallel velocity ($v_\parallel$)

The employed boundary condition for the parallel velocity to the magnetic field is a special case of the Chodura-Riemann condition [23] at the magnetic pre-sheath

$$v_\parallel = g(b_n) c_s \tag{8}$$

where $c_s \equiv \sqrt{\gamma k_B T / m_i}$ is the ion sound-speed, and $g(b_n)$ is a function of the normal projection of the magnetic field into the wall ($b_n \equiv \mathbf{B} \cdot \mathbf{n}/B$). Here $\mathbf{n}$ is a unit vector which is perpendicular to the boundary and points outside the plasma domain. The function g is needed to ensure that ions always flow towards the wall ($\mathbf{v}_\parallel \cdot \mathbf{n} > 0$) and that the variable $v_\parallel$ has a smooth transition in the regions where b_n changes sign. Otherwise the condition ($\mathbf{v}_\parallel \cdot \mathbf{n} > 0$) leads to discontinuities in $v_\parallel$ along the boundary that cannot be resolved (e.g. $v_\parallel$ would jump from c_s to $-c_s$). The chosen form of the g function is

$$g(b_n) = \mathrm{sign}(b_n) \left[\frac{1}{4} \left(1 + \tanh((|b_n| - g_1)/g_2)^2 \right) - g_3 \right] \tag{9}$$

and for this work the chosen coefficients are $(g_1, g_2, g_3) = (0.02, 0.016, 0.005754)$ such that $g(0) = 0$ and $g \approx 1$ when the angle of incidence is larger than 2°.

Heat flux

The boundary condition for the heat flux is based on reference [24]

$$\mathbf{q} \cdot \mathbf{n} = \gamma_{sh}\, n\, k_B T_e\, \mathbf{v}_\parallel \cdot \mathbf{n} + q_{min} \tag{10}$$

where n is the particle density and γ_{sh} is the sheath transmission coefficient. In this work the value $\gamma_{sh} = 11$ is chosen as it has been found in COMPASS through experimental observations for steady state plasmas [13]. Note that the evolution of γ_{sh} during disruptions is presently unknown. Since the boundary conditions for the parallel flow are such that $v_\parallel = 0$ when the field lines

are tangential to the wall (e.g. limiter point), a minimum heat flux (q_{min}) has been introduced. Otherwise, if $\mathbf{q}\cdot\mathbf{n}=0$ at the tangency points, the thermal energy would accumulate artificially at the boundary. We choose the minimum heat flux as $q_{min}=\gamma_{sh}n_e k_B T_e c_s \sin(\vartheta_{min})$, where unless explicitly stated, $\vartheta_{min}=2°$. The choice of a minimum value is also motivated by the reference [20], in which, perpendicular transport of energy and particles results in significant fluxes at grazing angles.

Ion flux

The employed boundary condition for the ion flux implies that ions leave the plasma domain at the parallel velocity

$$\mathbf{\Gamma}\cdot\mathbf{n}=n\mathbf{v}_{\parallel}\cdot\mathbf{n}+\Gamma_{min} \tag{11}$$

Similar to the heat flux boundary condition, we introduce a minimum particle flux to avoid artificial accumulation of particles, $\Gamma_{min}=nc_s\sin(\vartheta_{min})$.

Neutral particle flux

In order to ensure conservation of particles through the simulation the neutral particle flux is

$$\mathbf{\Gamma}_n\cdot\mathbf{n}=-\mathbf{\Gamma}\cdot\mathbf{n} \tag{12}$$

which implies that all ions leaving the boundary come back as neutral particles.

Electrostatic potential

Basic physics of the plasma implies that, in the presence of a sheath between the plasma and the material surfaces in contact with it, the maximum plasma current density that can flow along the field line is limited by the ion saturation current. Therefore in the presence of sufficiently large voltages induced by the disruption dynamics, the halo current could be directly determined by the ion saturation current. This hypothesis has been confirmed in recent COMPASS VDE experiments [1]. This was achieved by measuring independently the current flowing into the divertor through grounded Langmuir probes (to the vacuum vessel) and the ion saturation current at nearby locations with biased Langmuir probes. During disruptions, the parallel current density ($\mathbf{J}_{\parallel}$) was similar to the measured ion saturation current ($\mathbf{J}_{sat}$). Although the regime $J_{\parallel}\approx J_{sat}$ is found in these COMPASS tokamak disruptions, it cannot be concluded that in all tokamak disruptive plasmas $J_{\parallel}$ will reach the J_{sat} limit (i.e. $J_{\parallel}<J_{sat}$ could be possible). $J_{\parallel}$ and J_{sat} are driven by different physics mechanisms: voltage during the disruptions for $J_{\parallel}$ and edge plasma conditions, particularly plasma density, for J_{sat}. Therefore, there can be disruptive plasma conditions in which the limit imposed by J_{sat} on $J_{\parallel}$ plays no role on the halo current flow since $J_{\parallel}$ does not approach this limit. As we will show later, MHD models do not normally include this limitation of the current density and can violate it. For that reason we explore a suitable boundary condition for the MHD code JOREK including that limitation. The parallel current integrated over a field line has the following evolution in reduced MHD

$$\int_a^b \eta J_{\parallel} dl = -(\Phi_b-\Phi_a)-\int_a^b \frac{B_\phi}{R|B|}\frac{\partial\psi}{\partial t}dl \tag{13}$$

where a and b are respectively the starting and ending points of the field line and dl is the length differential along the field line. The latter relation is found by integrating the parallel electric field along the field line. For a given flux variation (e.g. caused by the decay of the plasma current) the current density along the field line is limited by the potential at its end points (Φ_b,Φ_a). Therefore the current density can be controlled by applying boundary conditions for Φ. At the plasma sheath, analytical expressions relating Φ and $J_{\parallel}$ that feature such a limit are well known from Langmuir probe theory [24]. The implementation of a boundary condition based on the Langmuir formulation is numerically very challenging and thus we have used a simplified boundary condition to limit the current to the ion saturation current

$$\Phi=\begin{cases}\Phi_w+\alpha(\mathbf{J}_{\parallel}-\mathbf{J}_{sat})\cdot\mathbf{n}, & \text{if}\quad \mathbf{J}_{\parallel}\cdot\mathbf{n}\geq\mathbf{J}_{sat}\cdot\mathbf{n}\\ \Phi_w, & \text{if}\quad \mathbf{J}_{\parallel}\cdot\mathbf{n}<\mathbf{J}_{sat}\cdot\mathbf{n}\end{cases} \tag{14}$$

where α is a constant. The boundary condition is such that when the parallel current ($\mathbf{J}_\parallel$) exceeds the ion saturation current ($\mathbf{J}_{sat}$), a voltage is driven with respect to the wall in order to reduce $\mathbf{J}_\parallel$. By choosing a large α it is ensured that the parallel current remains close to $\mathbf{J}_{sat}$. If $\mathbf{J}_\parallel \cdot \mathbf{n} < \mathbf{J}_{sat} \cdot \mathbf{n}$ the potential is set to the wall potential, which is chosen to be $\Phi_w = 0$ (the boundary acts as a perfect conductor in the poloidal direction).

The boundary condition for the potential can be expressed in terms of the JOREK variables. Assuming force-free balance in the open field- line region ($\mathbf{J} \times \mathbf{B} = 0$), the parallel current density is $\mathbf{J}_\parallel = -j\mathbf{B}/F_0$ with $j \equiv -RJ_\phi$ being the JOREK variable. The ion saturation current is $\mathbf{J}_{sat} = \mathrm{sign}(b_n)\, e\, n\, c_s\, \mathbf{b}$ and therefore the situation $\mathbf{J}_\parallel \cdot \mathbf{n} = \mathbf{J}_{sat} \cdot \mathbf{n}$ corresponds to $j = j_{sat} \equiv -\mathrm{sign}(b_n)\, e\, n\, c_s\, F_0/|B|$. Finally the JOREK boundary condition is

$$\Phi = \begin{cases} -\frac{\alpha}{F_0}(j - j_{sat})\mathbf{B} \cdot \mathbf{n}, & \text{if} \quad \mathbf{J}_\parallel \cdot \mathbf{n} \geq \mathbf{J}_{sat} \cdot \mathbf{n} \\ 0, & \text{if} \quad \mathbf{J}_\parallel \cdot \mathbf{n} < \mathbf{J}_{sat} \cdot \mathbf{n} \end{cases} \tag{15}$$

Vorticity and current density

In order to avoid second order derivatives in the code, auxiliary variables such as the toroidal vorticity $w_\phi = \frac{1}{F_0}\Delta\Phi$ and the toroidal current density $j = \Delta^*\psi$ are introduced. The boundary condition for the vorticity is simply $w_\phi = 0$ and j evolves according to Ampere's law ($j = \Delta^*\psi$).

Implementation

The heat and particle fluxes are implemented as natural boundary conditions of the finite element method. When performing the weak form and the partial integration of the $\underline{\mathbf{D}}$ and the $\underline{\boldsymbol{\kappa}}$ terms, the latter expressions for the fluxes are replaced in the arising boundary integrals. When Dirichlet boundary conditions are applied, a penalization method is used. The method can be interpreted as adding a boundary integral term to the governing equations. For example the following term is added to the parallel flow equation

$$\oint Z v^* (v_\parallel - g(b_n)c_s) dS \tag{16}$$

where v^* is a test function of the FEM, dS is the boundary surface and $Z = 10^{12}$ is an arbitrarily large value used to enforce the boundary condition.

3 Simulation setup

3.1 Equilibrium and steady state

In this subsection, we describe the plasma state prior to the VDE simulation. JOREK solves the Grad-Shafranov equation in order to obtain an initial condition that is accurate for the employed finite element method. In its free-boundary version, the computation of the equilibrium requires to specify the pressure and the toroidal current profiles as well as the geometry and the currents of the PF coils. An initial equilibrium was computed based on an EFIT [18] reconstruction of the COMPASS discharge #19172 at $t = 1090.0$ ms. As a kinetic version of EFIT was not available, the pressure profile was represented by a parabolic function. Similarly, the current profile is also parabolic, with the constraints that $q_{\mathrm{axis}} \sim 1$ and that the final total current is the experimental one ($I_p = 300$ kA). The currents flowing in the 5 independent circuits of the COMPASS PF coils are $(I_{\mathrm{BR}}, I_{\mathrm{BV}}, I_{\mathrm{EFPS}}, I_{\mathrm{MFPS}}, I_{\mathrm{SFPS}}) = (0.20, 2.00, -13.2, -7.16, -9.42)$ kA/turn. The I_{BR} circuit is used for feedback control on the vertical position and its current has been increased to 0.9 kA/turn in the simulation to obtain a more accurate matching of the vertical position of the magnetic axis (Z_{axis}).

For the plasma computational domain a polar grid has been chosen (see figure 1 (c)). The boundary of the grid matches the COMPASS first wall in the regions of main plasma-wall interaction. Its simplicity facilitates the implementation of the boundary conditions but some regions are not represented accurately. The grid features radial mesh accumulation at the computational boundary in order to resolve large temperature gradients that may arise. The vacuum vessel (blue curve in figure 1 (c)) is an axisymmetric version of the COMPASS wall and it is discretized in STARWALL with triangular elements using the thin wall approximation. The toroidal resistance of the wall is 40% smaller than the value given by COMPASS specifications ($\mathcal{R}_w = 0.63$ mΩ) in

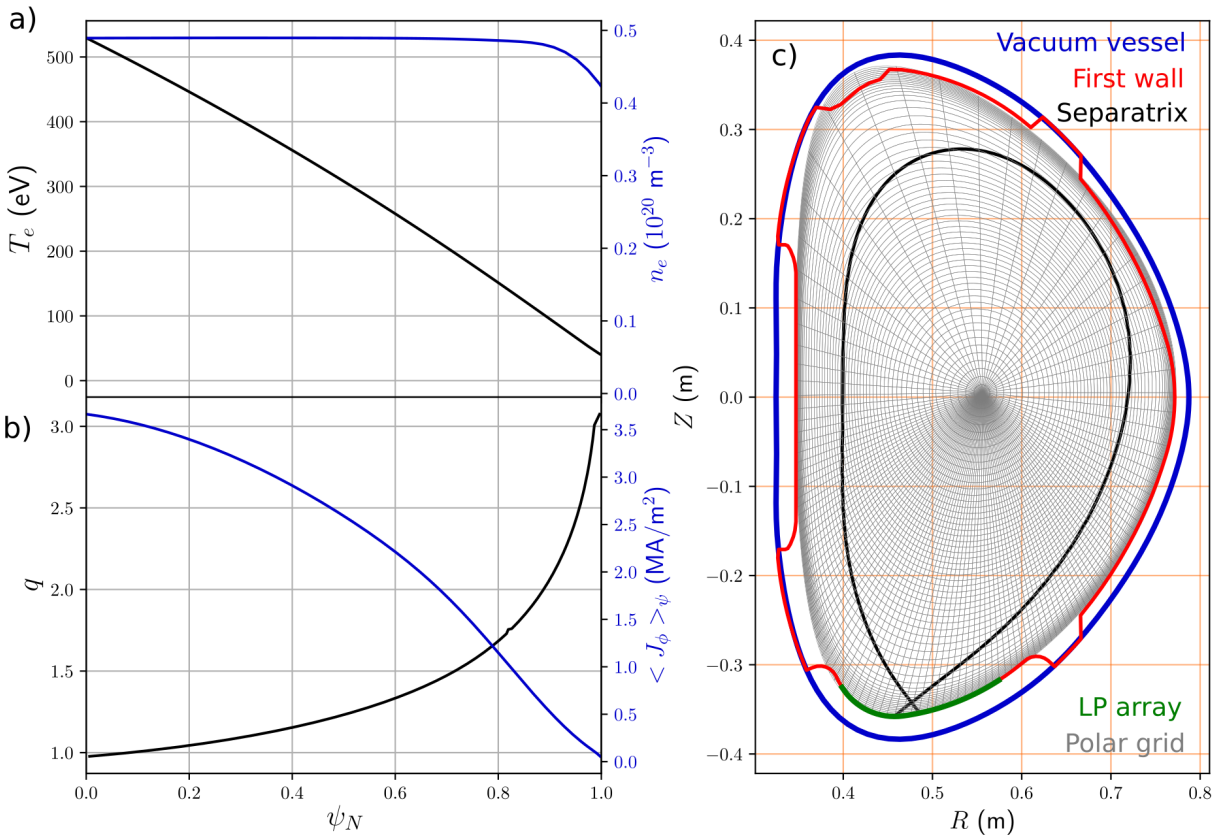

d)

I_p	$= 2.99 \times 10^{5}$ A	W_{mag}	$= 1.14 \times 10^{4}$ J	W_{thm}	$= 3.16 \times 10^{3}$ J
β_N	$= 6.58 \times 10^{-1}$ %	β_p	$= 1.37 \times 10^{-1}$	$l_i(3)$	$= 7.39 \times 10^{-1}$
q_0	$= 9.81 \times 10^{-1}$	q_{95}	$= 2.42$	V_p	$= 5.09 \times 10^{-1}$ m^3
R_{xpoint}	$= 4.77 \times 10^{-1}$ m	Z_{xpoint}	$= -3.42 \times 10^{-1}$ m	ψ_{xpoint}	$= -3.95 \times 10^{-3}$ Wb/rad
R_{axis}	$= 5.64 \times 10^{-1}$ m	Z_{axis}	$= 1.36 \times 10^{-2}$ m	ψ_{axis}	$= 1.65 \times 10^{-2}$ Wb/rad

FIGURE 1: Plasma configuration obtained after the steady state run in JOREK for the COMPASS shot #19172 at $t = 1090.0$ ms. (a) Temperature and density profiles at the midplane, (b) safety factor and averaged toroidal current density profiles as functions of the normalized poloidal flux. (c) Geometry of the COMPASS vacuum vessel and first wall, the Langmuir probe array location, the plasma separatrix and the polar grid used in JOREK. (d) List of relevant scalars describing the equilibrium.

order to have a better matching of the vertical position evolution with the experiment (see next section).

Once the initial condition is given, an axisymmetric time evolution simulation (of $\sim$ 4 ms) is performed in order to obtain a steady state plasma. The parameters that have been used for this phase are summarized in table 1. Note that we use temperature dependent η and $\kappa_\parallel$ with their corresponding Spitzer and Spitzer-Härm values. A current source term (ηj_0) is added to the magnetic flux equation in order to fix the initial current profile over time ($\partial_t \psi = ... + \eta(j - j_0)$). In the core, the steady state is reached when the Ohmic heating and the conductive perpendicular transport are balanced. The chosen $\kappa_\perp$ is such that the final thermal energy ($W_{th} = 3.2$ kJ) is similar to the energy obtained when mapping the Thomson scattering (n_e, T_e) measurements into the EFIT reconstruction assuming $T_i = 0.5 T_e$. The neutral diffusion coefficient was taken from JOREK simulations without charge exchange that were compared to SOLPS-ITER simulations [22]. The ion and neutral particle densities are in equilibrium when the diffusive transport and the ionization and recombination processes are balanced. The final core profiles are shown in figure 1 (a) and (b). With the chosen parameters, the electron density accumulates at the High Field Side (HFS) near the lower X-point (see Figure 2 right), which explains the increasing plasma density towards the separatrix seen in Figure 1 (a). The final plasma temperature profile is also shown in Figure 2 (left) and several parameters describing the final steady state equilibrium are presented in Figure 1 (d).

Parameter	Value	Description
D	4.57 m^2/s	Isotropic particle diffusion coefficient
D_n	228 m^2/s	Isotropic neutral particle diffusion coefficient
$\kappa_\perp$	0.988×10^{20} $(\mathrm{m\ s})^{-1}$	Perpendicular thermal conductivity
$\kappa_\parallel = \kappa_0 (T_e/T_{e0})^{5/2}$	$\kappa_0 = 3.73 \times 10^{29}$ $(\mathrm{m\ s})^{-1}$	Parallel thermal conductivity
$\eta = \eta_0 (T_e/T_{e0})^{-3/2}$	$\eta_0 = 4.19 \times 10^{-8} \Omega$ m	Resistivity
$(\mu_\parallel, \mu_\perp)$	$(3.48, 1.05) \times 10^{-7}$ kg/(m s)	Parallel/perpendicular dynamic viscosity
γ_{sh}	11	Sheath transmission coefficient

TABLE 1: Parameters used during the steady state run. For the temperature dependent parameters the reference temperature is $T_{e0} = 1$ keV. Note that except for η and $\kappa_\parallel$ the coefficients are spatially constant.

3.2 Triggering of the VDE

During the steady state run, vertical position control is achieved with a PID controller acting on the I_{BR} PF coil circuit. In the experiments a vertical kick is performed by applying a current wave-form to the I_{BR} circuit in order to force a downwards VDE. In the simulation the same PF coil current variation (ΔI_{BR}) as in the experiment is specified and leads to a similar vertical position evolution (see figure 3). We remind the reader that we have reduced the wall resistance by 40% in order to have a better matching with the experiment. The case with the COMPASS real wall resistance is also present in figure 3 showing a faster plasma displacement modelled by JOREK than measured in the experiment. Discrepancies between experiment and modeling may originate from equilibrium reconstruction uncertainties (e.g. choice parabolic profiles) and from the simplification of conducting structures (i.e. we model the complex COMPASS vessel as a thin axisymmetric wall). For the VDE phase, the employed parameters were not modified with respect to the steady state phase. The main difference is that the current source term is switched-off and the current is allowed to decay. Also the code is run in axisymmetric mode.

3.3 VDE regime and total halo currents

The chosen COMPASS disruption (shot #19172) is considered as a *hot* VDE disruption. In *hot* VDEs, the vertical motion precedes the current quench phase (see the experimental Z_{axis} and I_p time traces in figure 3). The largest wall forces and halo current fractions are typically observed for this type of events [10]. The total poloidal halo current ($I_{halo,pol}$) found in the base simulation of this paper is compared with the experimental value in figure 4 (see blue and red lines in the subplot c). The experimental value corresponds to the measured poloidal vessel current obtained

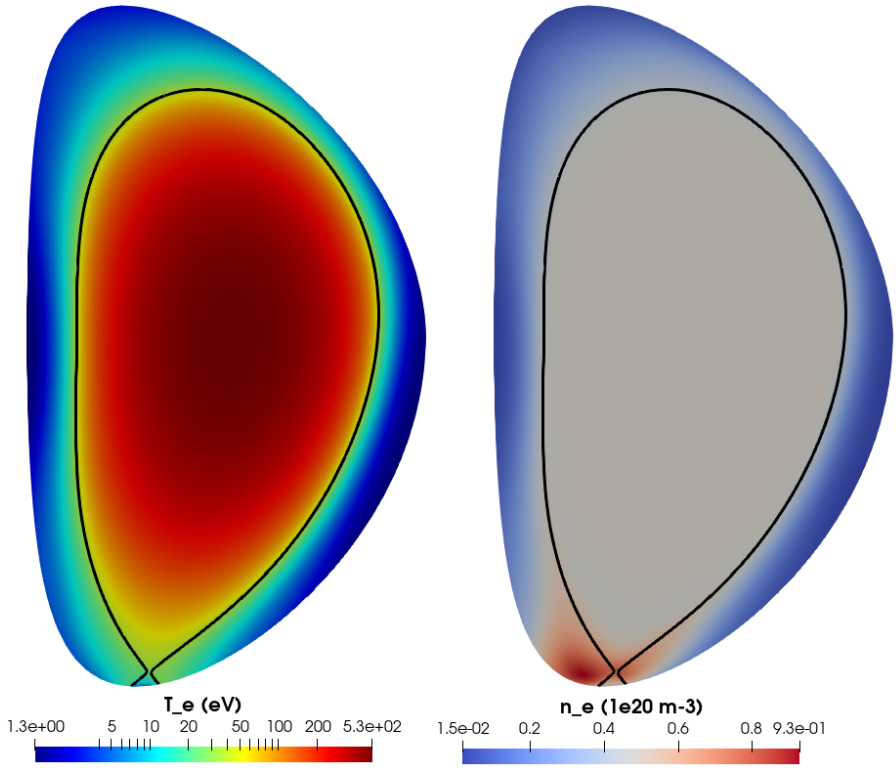

FIGURE 2: Electron temperature distribution in logarithmic scale (left) and electron density distribution in linear scale (right) at the end of the steady state run. The separatrix is indicated by the black curve.

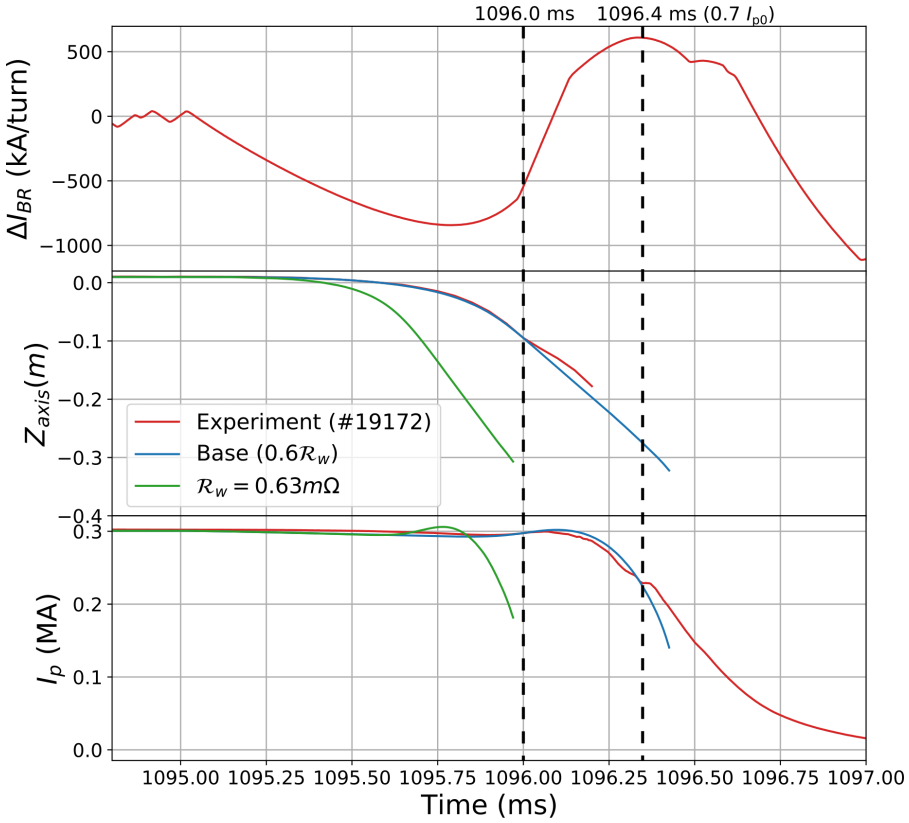

FIGURE 3: Comparison of two JOREK runs with different wall resistances (blue and green lines) and the experimental time traces (red). (Top) Current change in the I_{BR} circuit. (Middle) Vertical position of the magnetic axis. (Bottom) Total plasma current inside the plasma domain. The vertical dashed lines indicate the two times (t = 1096.0 ms) and (t = 1096.4 ms) that are chosen in sections 5 and 6 to plot the divertor profiles.

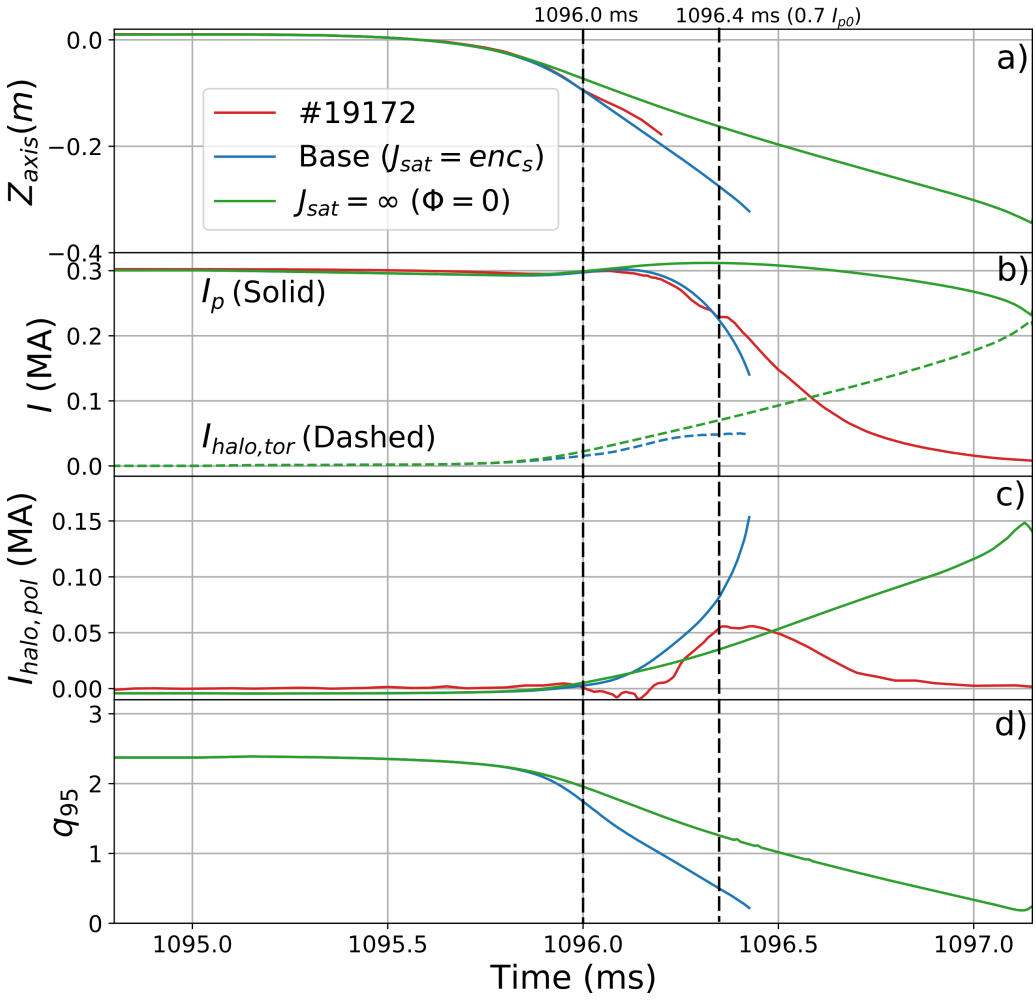

FIGURE 4: Comparison of two simulations with a different J_{sat} value used for the boundary condition given by expression 15 and the experimental time trace (in red). (a) Vertical position of the magnetic axis. (b) Total toroidal plasma current (solid) and toroidal halo current (dashed). (c) Total poloidal halo current. The experimental value is inferred from poloidal wall current measurements and it is a lower estimate of the total poloidal halo current (see text). (d) Edge safety factor. The figure shows the stabilizing effect of the halo currents and the large influence of the boundary condition for Φ for the dynamics of the VDE.

with Mirnov coil measurements [16]. The maximum experimental value for the halo fraction (i.e. the poloidal halo current normalized by the pre-disruptive plasma current) is HF = 0.19. However, a recent analysis (to be published) shows that this may be a lower bound of the real value. A conducting backplate connecting the COMPASS divertor to the vacuum vessel is likely to be short-circuiting an important fraction of the halo currents. Therefore these short-circuited halo currents could be missed by the vacuum vessel measurements. An upper estimate of the non-measured currents was done by integrating the current density measured with divertor Langmuir probes (see section 5), which resulted in total halo fractions in the range of HF =0.19-0.29.

The simulated toroidal halo current saturates to a maximum value of about 50 kA (see blue-dashed line in figure 4 b). However the poloidal halo current increases rapidly after the toroidal current saturation. This is due to the fast drop of the edge safety factor (see figure 4 d). Note that toroidal and poloidal halo current components are related by the effective safety factor in the halo region ($I_{halo,pol} \sim I_{halo,tor}/q_{eff}$ [14]). Since the simulations for the present work are axisymmetric, the edge safety factor (q_{95}) is not constrained by a lower limit. By MHD stability considerations, it is expected that 3-dimensional MHD activity would limit the minimum q_{95} to values in the range of 1 or 2. This shows the need of simulating these events including 3-dimensional effects. Our future work will combine the model advancements presented here with such 3D simulations.

Assuming an experimental $q_{eff} \sim 2$, the toroidal halo currents are expected to be in the order of 100 kA. The maximum experimental loop voltage observed during the disruption is 63 V, which is consistent with simulated loop voltages of 75 V at $t = 1096.4$ ms. Accordingly, the effective resistance of the halo current is estimated to be $\mathcal{R}_{eff} \sim V_{loop}/I_{halo,tor} = 0.63\,\mathrm{m\Omega}$. The poloidal resistance of the entire vessel is 0.25 mΩ. Since halo currents are expected to flow on a fraction of the poloidal contour of the vessel, the effective vessel resistance is expected to be of the order of 0.1 mΩ or lower. Therefore the halo current must be dominated by the plasma and the sheath resistances ($\mathcal{R}_{eff} = \mathcal{R}_{halo} + \mathcal{R}_{sheath}$). Using the magnetic field from the simulations it is found that for $T_e = 10$ eV, the halo current resistivity is $\mathcal{R}_{halo} \sim 0.25\,\mathrm{m\Omega}$. Thus we estimate that the halo and sheath resistances are of the same order for these discharges.

4 Influence of boundary conditions

4.1 Electric potential and ion saturation current

The boundary condition given by expression 15 is tested in this subsection and compared to the usual boundary condition applied in MHD simulations. When the usual MHD boundary condition for the electrostatic potential $\Phi = 0$ is applied, large halo currents are induced in the SOL and the decay time of the plasma current is much longer than observed in the experiment (see green and red lines of Figure 4). In this case the halo current has a very large width and presents a non-monotonic profile as indicated by Figure 5 b), in which, the toroidal current density is shown at a late time of the VDE. A broad halo width (w_{halo}) decreases the total resistance of the halo region ($\mathcal{R}_{halo} \sim \eta_{halo}/w_{halo}$) and consequently the total plasma current decays at a slower rate. Since in our simulations the core and the halo regions are treated with the same formalism, the full plasma domain acts as a conductor with resistivity $\eta(T_e)$. Due to the electric field created by the moving plasma core, currents appearing in the far SOL (Figure 5 b) can be self-sustained through Ohmic heating (which increases T_e and makes the region more conductive).

The case with the boundary condition $\Phi = 0$ leads to non-physical results since the normal current density ($\mathbf{J} \cdot \mathbf{n}$) largely exceeds the ion saturation current ($\mathbf{J}_{sat} \cdot \mathbf{n}$) at different locations along the plasma-wall interface (see Figure 6). In order to visualize these quantities along the boundary of the plasma domain, the polar coordinate θ_w is introduced. The polar coordinate system is centered at $(R, Z) = (0.56, 0)$ m such that $\theta_w = 0$ corresponds to the outer midplane ($Z = 0$). The results shown in Figure 6 imply that the usual boundary condition ($\Phi = 0$) allows large currents to flow at locations with very low plasma densities (e.g. at $\theta_w/2\pi = 0.6$ near the high field side midplane).

When the boundary condition given by equation 15 is applied for the electrostatic potential, the halo current is limited by the ion saturation current. Since the limitation is given by $J_{sat} \equiv enc_s$, the halo current is mainly constrained by the particle density profile (n) which evolves according to ionization, recombination, diffusion and convection. In practice, this implies that the halo current cannot be induced in the far SOL regions where the particle density is low. The latter can be observed in Figure 5 a) as well as in Figure 7. As a consequence, the total induced halo

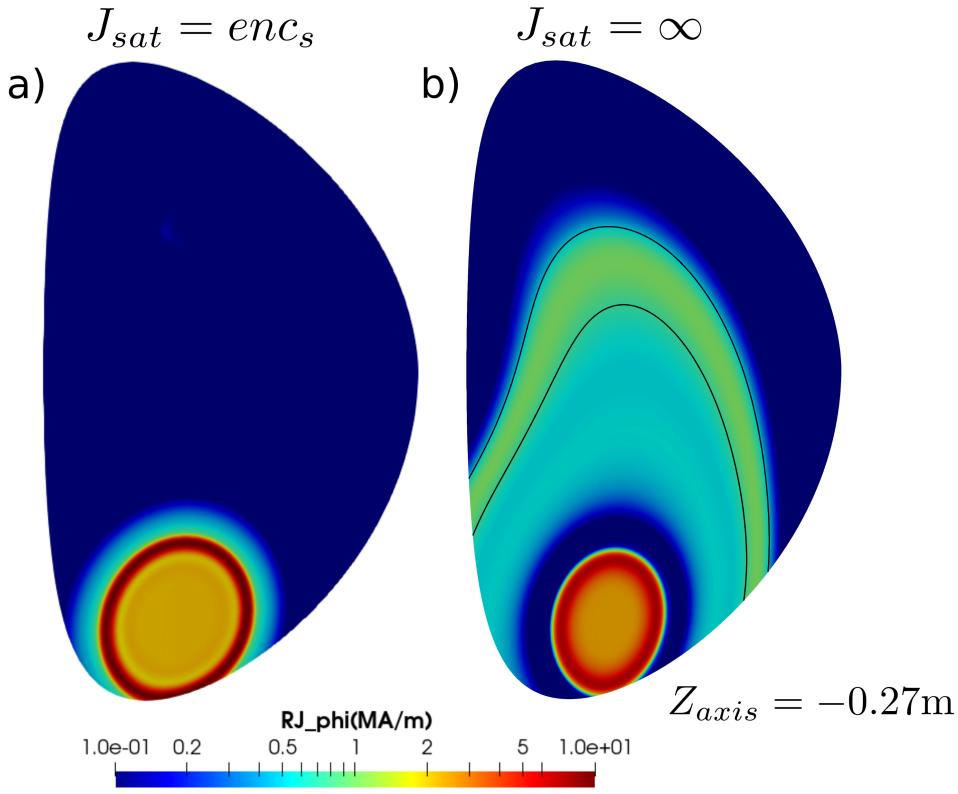

FIGURE 5: Toroidal current density at $Z_{axis} = -0.27$ m for the same two simulations as in Figure 4 with different boundary conditions for the electrostatic potential. (a) Simulation with $J_{sat} = enc_s$ and Φ employed in expression 15. (b) Simulation with $\Phi = 0$ as boundary condition (equivalent to use $J_{sat} = \infty$ in expression 15). The figure shows the large influence of the boundary condition for Φ on the distribution of the halo currents. The black lines in figure (b) delimit a flux tube in the far SOL with a large current density ($J_{\|} \sim 2$ MA/m^2).

current is much smaller than in the case without current limitation (see blue and green lines of Figure 4). The halo current width is also severely reduced (by about a factor of 4 at the outer midplane as shown in Figure 5) and thus the total plasma current decays at a faster rate, which is closer to experimental observations. Therefore the performed simulations show that the boundary condition for the electrostatic potential (Φ) plays a very significant role for both plasma dynamics and distribution of the current profile in the halo region (see Figure 7).

The boundary condition shown in equation 15 provides an upper limit only for the positive current ($\mathbf{J}\cdot\mathbf{n} > 0$), which in this case is induced by the VDE at the High Field Side (HFS). In the Low Field Side (LFS), the normal current density is negative and therefore it might be eventually limited by the electron saturation current which is a factor $\sqrt{m_i/m_e} \approx 61$ larger than the ion saturation current. The limit to negative current in the LFS is not driven by the electron saturation current but by the limit to the ion saturation current on the HFS and electric charge conservation of the plasma, which leads to a similar negative current to J_{sat} on the LFS despite the $\Phi = 0$ boundary condition there.

Note that in the green shaded region of Figure 7 the halo current is somewhat larger than the ion saturation current in the simulations. Unfortunately, the current could not be limited near the contact point or limiter point (green region) for the following reasons. Around the contact point (defined by $\mathbf{B}\cdot\mathbf{n} = 0$), large gradients of the electrostatic potential are formed along the boundary ($\boldsymbol{\nabla}_{\tan}\Phi$). The latter is due to the fact that at exactly the contact point $\Phi = 0$, and in its vicinity, large voltages are applied in order to limit the parallel current (since $\mathbf{B}\cdot\mathbf{n} \neq 0$). Since the parallel current density can locally increase due to these gradients via the local Ohm's law ($J_\parallel \propto -\mathbf{B}\cdot\boldsymbol{\nabla}\Phi/\eta$), an unstable situation can occur around this point. In this case, an increase of $J_\parallel$ near the limiter point raises $\mathbf{B}\cdot\boldsymbol{\nabla}\Phi$, which in turn increases $J_\parallel$ even further. To avoid this issue, the following boundary condition is imposed to control the gradient in Φ along the boundary

$$\Phi = -D_{lim}\frac{\partial\Phi}{\partial l} \tag{17}$$

where D_{lim} is the distance in real space to the contact point and l is the length along the boundary. The latter boundary condition is applied up to 6 cm away from the limiter point, which is the minimum stable distance that has been found by a trial and error analysis. The effect of this boundary condition on the electrostatic potential can be observed in the green region of figure 7. Due to the special treatment of Φ in the vicinity of the contact point, the maximum current density exceeds the ion saturation current by up to ~30% of its value (see the $\mathbf{J}\cdot\mathbf{n}$ and $\mathbf{J}_{sat}\cdot\mathbf{n}$ profiles at $t = 1096.4$ ms in Figure 7). Therefore, our simulations would overestimate the maximum current density by about 30% in this region compared to the experiment in the worst case presented here. Future works will consider stabilization techniques for the boundary condition (15) to strictly ensure $\mathbf{J}\cdot\mathbf{n} \leq \mathbf{J}_{sat}\cdot\mathbf{n}$ at the contact point.

Finally we investigate the origin of the non-monotonic current profile for the case with $\Phi = 0$. Assuming spatially constant T_e, $J_\parallel$ and n and that the Ohmic heating and the parallel conduction are dominant, the evolution of the temperature in a SOL flux tube is

$$\frac{\partial T_e}{\partial t} \approx \frac{\eta J_\parallel^2}{n} - c_{sh}T_e^{3/2}\frac{A_{tube}}{V_{tube}} = \left(\eta_0 T_0^{-3/2}\frac{E_\parallel^2}{n} - c_{sh}\frac{A_{tube}}{V_{tube}}\right)T_e^{3/2} \tag{18}$$

where V_{tube} is the volume of the flux tube, A_{tube} is the cross-sectional area of the flux tube at its end points, $c_{sh} \equiv 2\gamma_{sh}\sqrt{\gamma k_B^3/m_i}$ and we have used that $E_\parallel = \eta J_\parallel$. The latter equation shows that for a given $E_\parallel$ the flux tubes with smaller density and with smaller A_{tube}/V_{tube} ratios are the most efficient ones for increasing T_e. These conditions correspond to flux tubes in the far SOL (see the black lines in figure 5 b) that delimit such a flux tube). That is the reason why the current is preferentially induced on those regions and a non-monotonic profile is observed in Figure 5 b).

4.2 q_{min} and Γ_{min}

In order to test the influence of q_{min} and Γ_{min}, two different simulations were run with $\vartheta_{min} = 1°$ and $\vartheta_{min} = 2°$. The influence of ϑ_{min} on the vertical position and current decay is not significant, but the T_e near the contact point can be increased by 25% when $\vartheta_{min} = 1°$ (see figure 8).

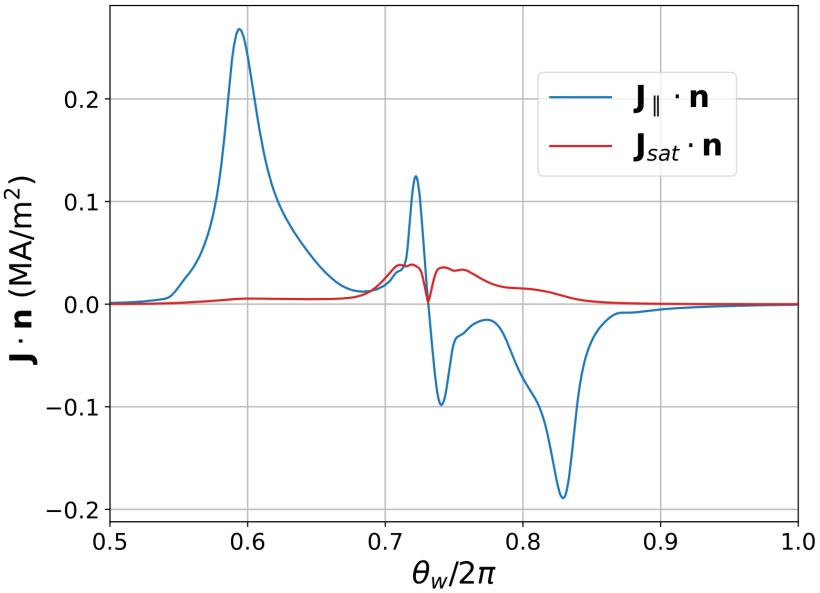

FIGURE 6: Normal current and ion saturation current density at the wall-plasma interface as function of the polar angle (θ_w) for the simulation with $\Phi = 0$ at the time when $Z_{axis} = -0.27$ m. The figure shows that the parallel current density becomes larger than the ion saturation current for the usual MHD boundary condition, violating the experimentally found physical limit.

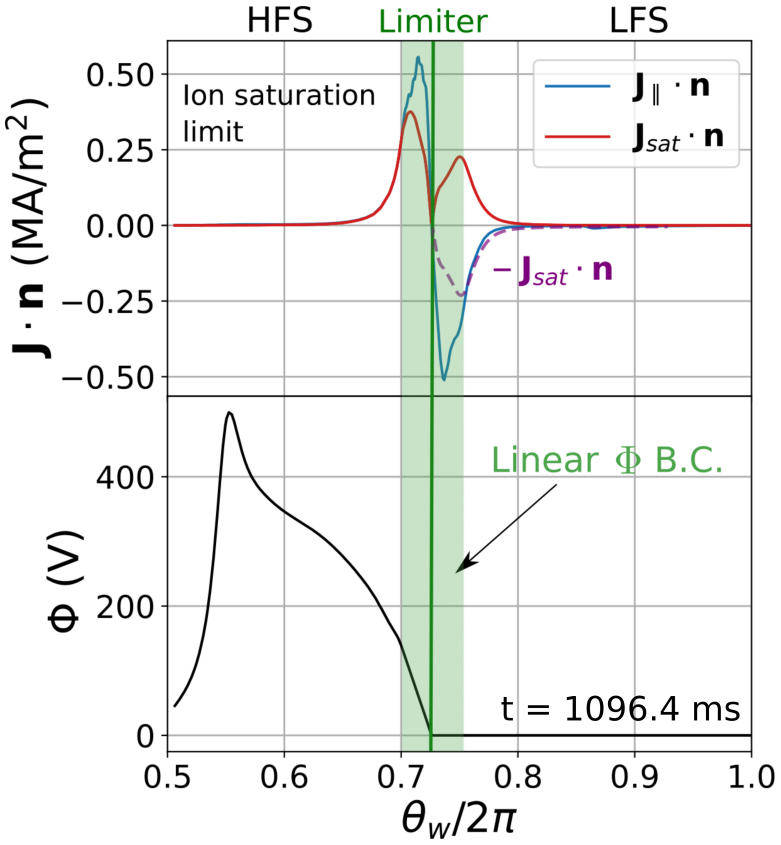

FIGURE 7: (Top) Normal current and ion saturation current density at the wall-plasma interface as function of the polar angle (θ_w) for the "Base" VDE simulation at $t = 1096.4$ ms and $Z_{axis} = -0.27$ m. The limiter point is indicated by the green line and the green area is the region where linear boundary conditions are applied for Φ. The purple dashed line is $-\mathbf{J}_{sat} \cdot \mathbf{n}$ at the Low Field Side (see text for the physical limitations to negative current in the LFS). (Bottom) Electrostatic potential as a function of θ_w.

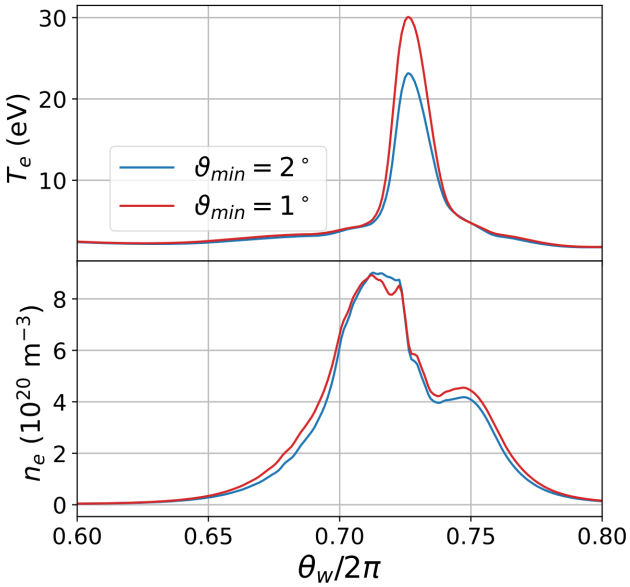

FIGURE 8: T_e and n_e profiles along the wall for two different ϑ_{min} values used in equations (10) and (11) at $I_p = 0.7 I_{p0}$.

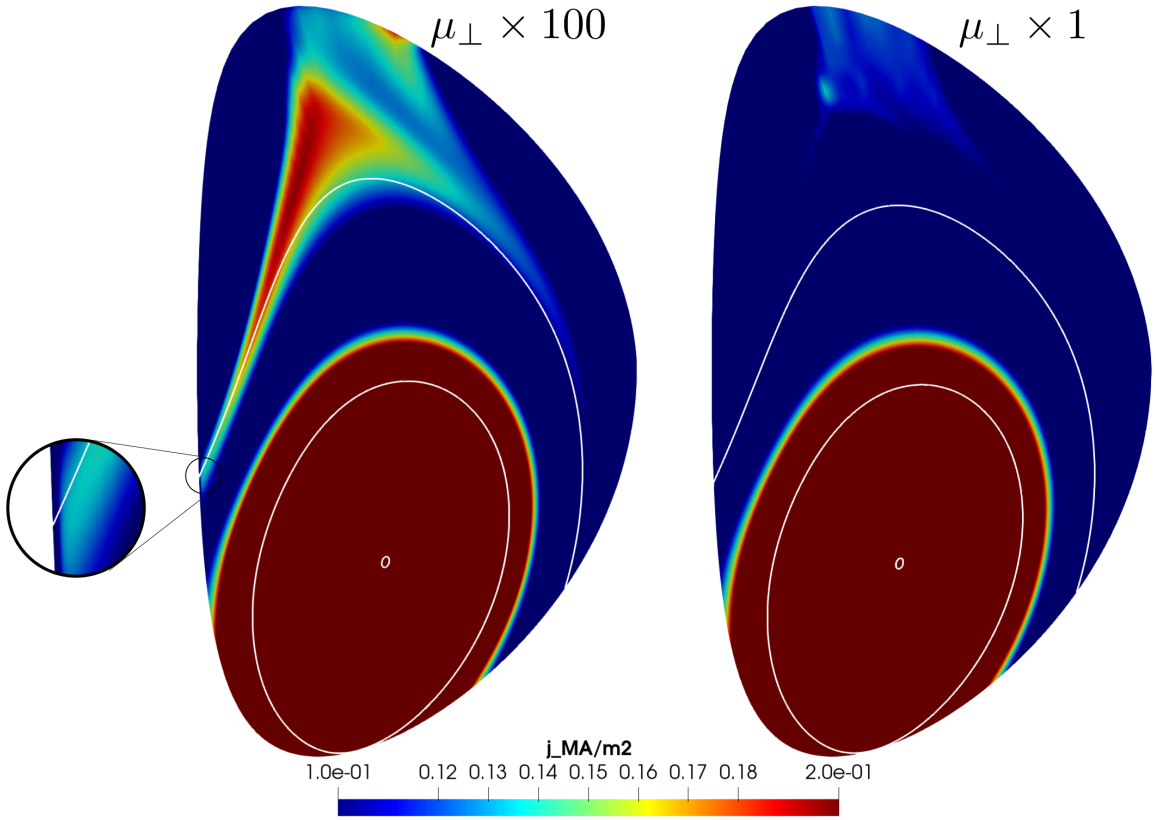

FIGURE 9: Current density in the far SOL in (left) simulation with $\mu_\perp = 1.05 \times 10^{-5}$kg m/s and (right) simulation with $\mu_\perp = 1.05 \times 10^{-7}$kg m/s. The viscosity coefficients are spatially constant. The white contours indicate three different flux surfaces. When a large unphysical viscosity is present, current gradients along the field lines can be sustained.

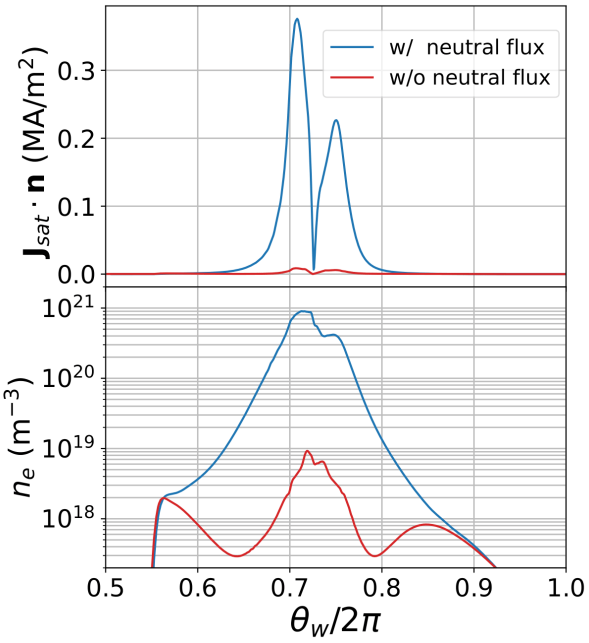

FIGURE 10: Normal ion saturation current density (top) and electron density (bottom) at the wall-plasma interface as function of the polar angle (θ_w) for the time when $Z_{axis} = -0.27$ m. The blue line corresponds to the Base VDE simulation and the red line to a VDE case in which the neutral particle flux has been set to zero ($\mathbf{\Gamma}_n \cdot \mathbf{n} = 0$). The figure shows the importance of including neutral particles to calculate the electron particle density and the ion saturation current at the plasma-wall interface.

4.3 Effect of viscosity on ion saturation current boundary condition

The choice of the plasma perpendicular viscosity is found to play a very important role in the limitation of $J_\parallel$. Near Alfvenic equilibrium and for cold plasmas, the current density is parallel to the magnetic field lines ($\mathbf{J} \times \mathbf{B} = 0$). In the absence of charge accumulation ($\boldsymbol{\nabla} \cdot \mathbf{J} = 0$), the current density also satisfies

$$\mathbf{B} \cdot \boldsymbol{\nabla}(J_\parallel / B) \approx \frac{1}{F_0} \mathbf{B} \cdot \boldsymbol{\nabla} j = 0 \tag{19}$$

which implies that the quantity $j \equiv R J_\phi$ is approximately constant along the magnetic field-lines. When the boundary condition for Φ is applied, the current density at the boundary is locally limited by J_{sat}. This creates a gradient of current along field-lines leading to the excitation of Alfven waves which restore $\mathbf{B} \cdot \boldsymbol{\nabla} j = 0$. For time-scales longer than the Alfven time, gradients along the field-lines must vanish implying that $J_\parallel \leq J_{sat}|_{wall}$. In the presence of unphysically large fluid viscosities, a balance between the viscous force and the current gradient force can be established ($\mathbf{B} \cdot \boldsymbol{\nabla} j \approx \mu_\perp \Delta w$). Such a balance can prevent the excitation of Alfven waves and the homogenization of the current along the field-lines leading to $J_\parallel > J_{sat}|_{wall}$. A case with large viscosity is presented in figure 9 (left) showing the strong effect of the viscosity in the SOL current profile and the existence of large current density gradients along field-lines. Therefore special care must be taken with the viscosity choice when applying this type of boundary conditions. To prevent unphysical results in our simulations, the value of $\mu_\perp$ has been chosen small enough to avoid gradients of current density and such that a smaller value does not influence the plasma dynamics.

4.4 Effect of the neutral particle flux

In this subsection we discuss the large effect of neutral particles on the electron density and on the ion saturation current. The VDE simulation was restarted from the end of the steady state run and the neutral particle flux was to zero ($\mathbf{\Gamma}_n \cdot \mathbf{n} = 0$). For that case, the electron density and the ion saturation current is compared to the Base simulation at a latter phase of the VDE in Figure 10. When the neutral particle flux is set to zero, the plasma ions leave the computational domain at the sound speed and do not come back as neutral particles. Therefore the boundary acts as a large ion sink that leads to plasma densities lower than the Base simulation by two orders of magnitude

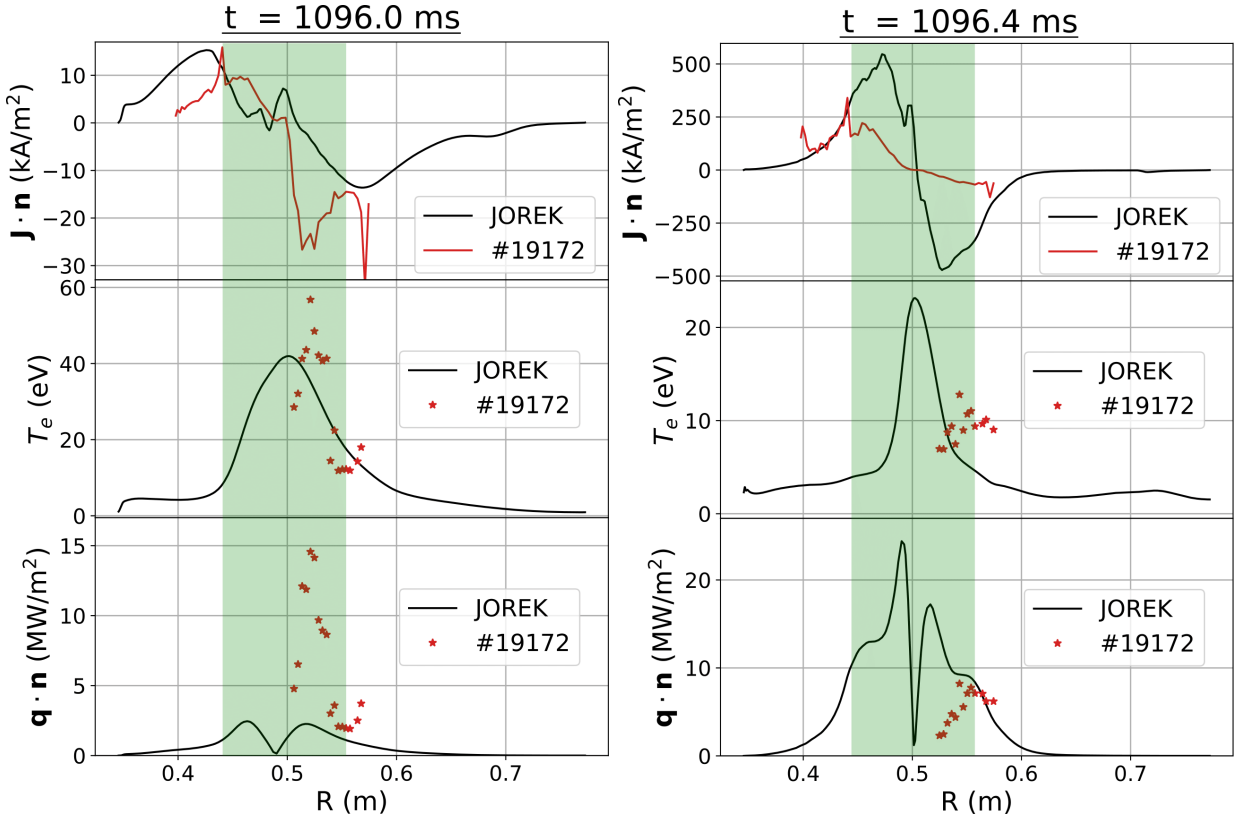

FIGURE 11: Normal current density, electron temperature and normal heat flux on the divertor at (left) $t = 1096.0$ ms and at (right) $I_p = 0.7 I_{p0} = 0.21$ MA ($t = 1096.40$ ms in the experiment and $t = 1096.38$ ms in JOREK). The JOREK results for the Base VDE simulation are shown in black and the experimental measurements in red. The experimental heat flux has been estimated with $q_{\parallel} \approx \gamma_{sh} T_e[\text{eV}] |J_{\parallel}|$ and $\gamma_{sh} = 11$. The shaded region in green corresponds to the area where the J_{sat} limitation of the current density is not effective and a linear boundary condition is applied for the electrostatic potential as explained in section 4.1. Experimental uncertainties in the current density and temperature measurements are of the order of 5% and 15% respectively.

(see Figure 10). As a consequence, the ion saturation current density is strongly reduced and halo currents cannot be induced during the VDE. The latter demonstrates that neutral particles must be included when using sheath boundary conditions in order to a obtain a self-consistent evolution of the plasma density and the ion saturation current at the plasma-wall interface.

5 Comparison with divertor probe measurements

For the COMPASS experimental campaign on VDEs and current flows, two arrays of rooftop-shaped Langmuir probes (LPs) and one array of Ball-pen probes (BPPs) [2] were used to measure the parallel current density and the electron temperature at the lower divertor. The location of the LPs array along the divertor is indicated in figure 1 (c). Since during COMPASS disruptions it is found that $J_{\parallel} \approx J_{sat}$, the experimental heat-flux can be estimated by $q_{\parallel} = \gamma_{sh} T_e[\text{eV}] J_{sat} \approx \gamma_{sh} T_e[\text{eV}] |J_{\parallel}|$. Note however that this estimation is given for reference and that γ_{sh} is assumed to be 11 while it could vary significantly during the disruption since strong halo currents circulate in the SOL. In figure 11, the JOREK values are compared to the experimental results along the boundary at two different times.

After a downwards motion of 10 cm and before the decay of the plasma current ($t = 1096.0$ ms), the simulation shows current and temperature values in a similar range to those observed in the experiments (figure 11 left). The location of the contact point in the simulation ($R_{lim} = 0.490$ m) is in good agreement with the experimental location defined by $J_{\parallel} = 0$ ($R_{lim} = 0.499$ m). The JOREK current profile is broader in the HFS than in the experiment, but due to the short width of the LP array it is not possible to conclude the same at the LFS. The large power flux in the experiment compared to JOREK is most likely due to the fact that the thermal quench is taking

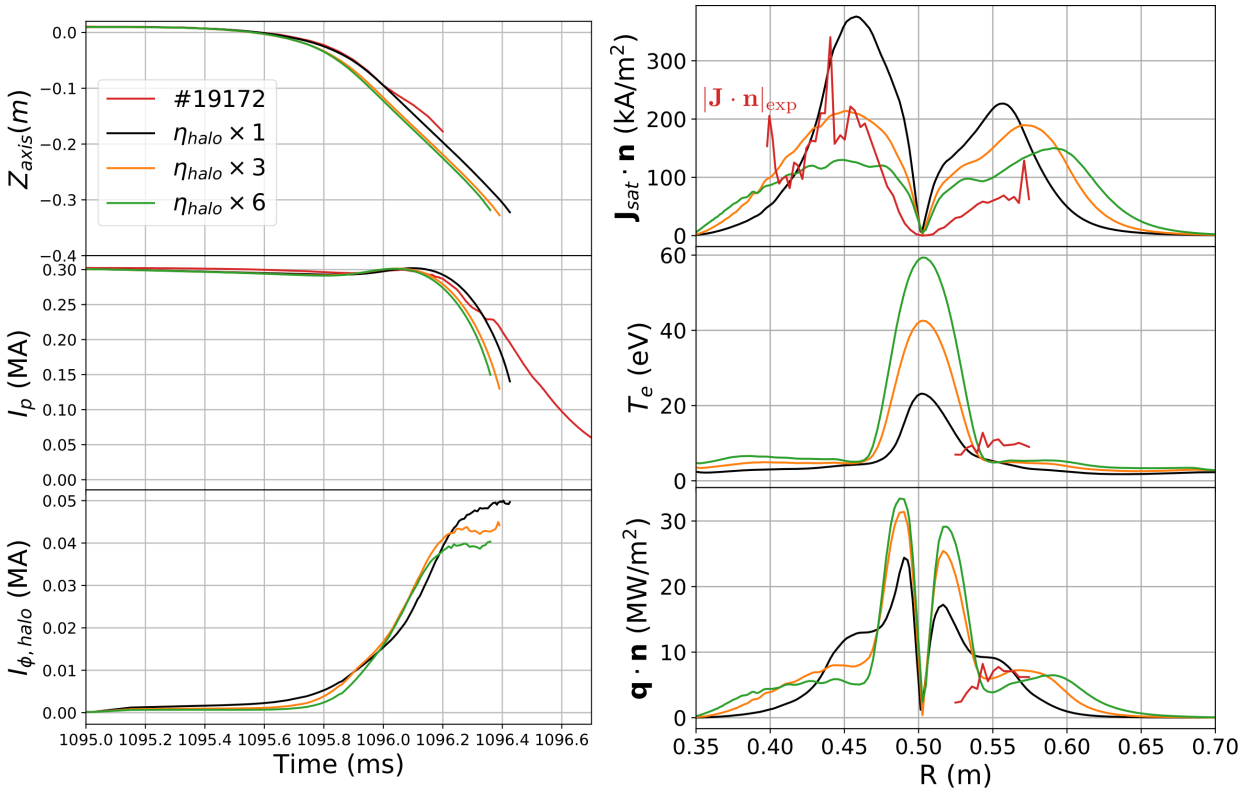

FIGURE 12: (Left) Vertical position of the magnetic axis, total toroidal plasma current and toroidal halo current in the plasma as function of time. (Right) Normal ion saturation current density, electron temperature and normal heat flux on the divertor at $I_p = 0.7 I_{p0} = 0.21$ MA as function of the major radius. The lines with different colors correspond to simulations with different factors multiplying the plasma resistivity in the halo region. Note that in the upper right figure the absolute value of the experimental current density (red line) is plotted for reference.

place at 1096.0 ms in the experiment (as indicated by H_α measurements) while such a quench is not included in this axisymmetric JOREK simulations.

In figure 11 (right) the same quantities are compared at the time where the total current reaches 70% of its pre-disruptive value in the experiment and in the simulation. Excellent agreement is found on the location of the limiter position ($R_{lim} = 0.50$ m). This particular time point is chosen because the current densities reach their maximum values ~ 2 MA/m^2. The experiments indicate that at this point, the temperatures decay to ~ 10 eV and that the heat-flux is significantly reduced. For the JOREK Base simulation, a thermal quench was not triggered artificially and cannot occur self-consistently due to the axisymmetric simulation setup, thus at this point, the plasma core still contains 28% of its pre-disruptive thermal energy. Due to the large pressures around the limiter point, the JOREK results show large heat fluxes compared to the experiments. However, where $J_\parallel$ is limited by J_{sat} in the simulation, similar current densities and temperatures are found, although the JOREK simulations show that T_e falls with a smaller decay length. We remind that in the vicinity of the contact point, the maximum $\mathbf{J} \cdot \mathbf{n}$ exceeds $\mathbf{J}_{sat} \cdot \mathbf{n}$ by about 30% due to the issues explained in section 4.1 (see also Figure 7). The influence of several simulation parameters onto the results is shown in the next section.

6 Sensitivity to different parameters

In this section we study how the different parameters shown in table 1 influence the profiles at the divertor region. During all simulated cases, the parallel current was always found to be limited by the ion saturation current (except for $R \in [R_{lim} - 0.06, R_{lim} + 0.06]$). Therefore when analyzing the current density profile we focus on how different parameters can affect the amplitude and shape of the J_{sat} profile.

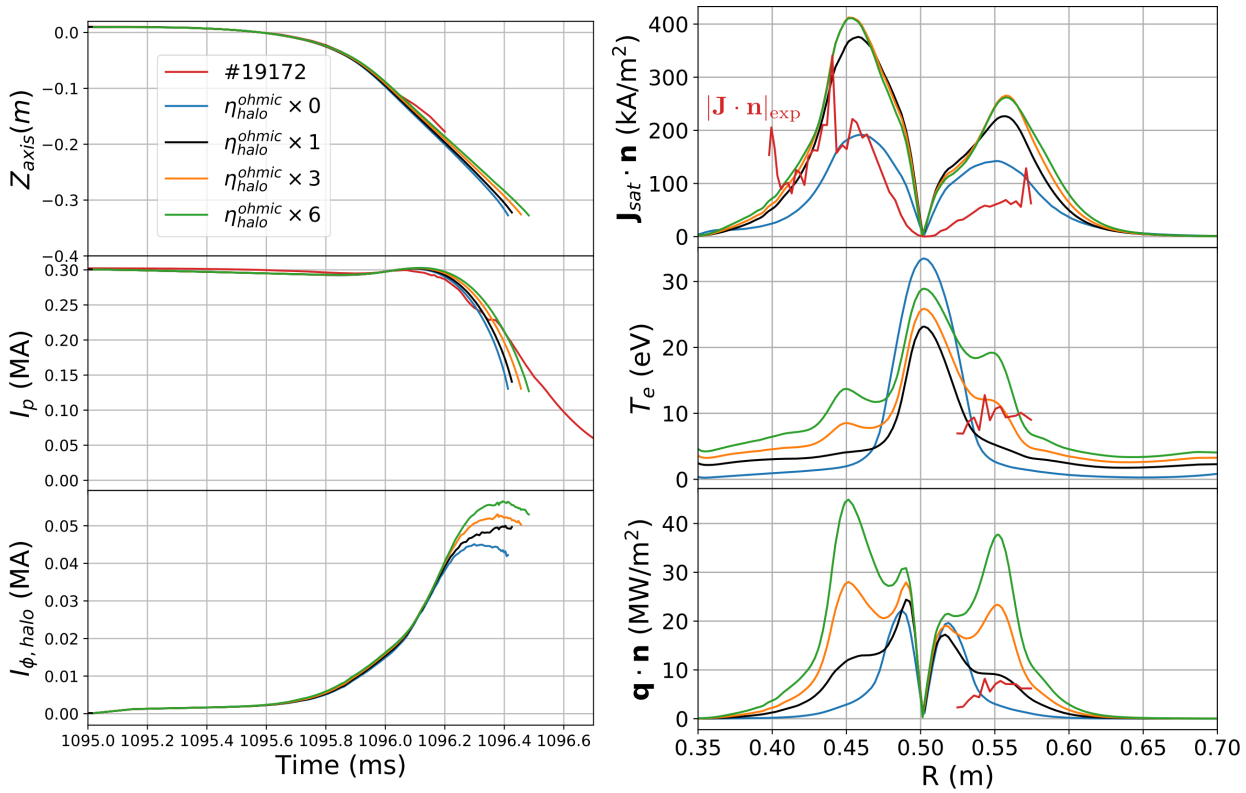

FIGURE 13: (Left) Vertical position of the magnetic axis, total toroidal plasma current and toroidal halo current in the plasma as function of time. (Right) Normal ion saturation current density, electron temperature and normal heat flux on the divertor at $I_p = 0.7 I_{p0} = 0.21$ MA as function of the major radius. The lines with different colors correspond to simulations with different factors multiplying the Ohmic heating term in the halo region without modifying current diffusion. Note that in the upper right figure the absolute value of the experimental current density (red line) is plotted for reference.

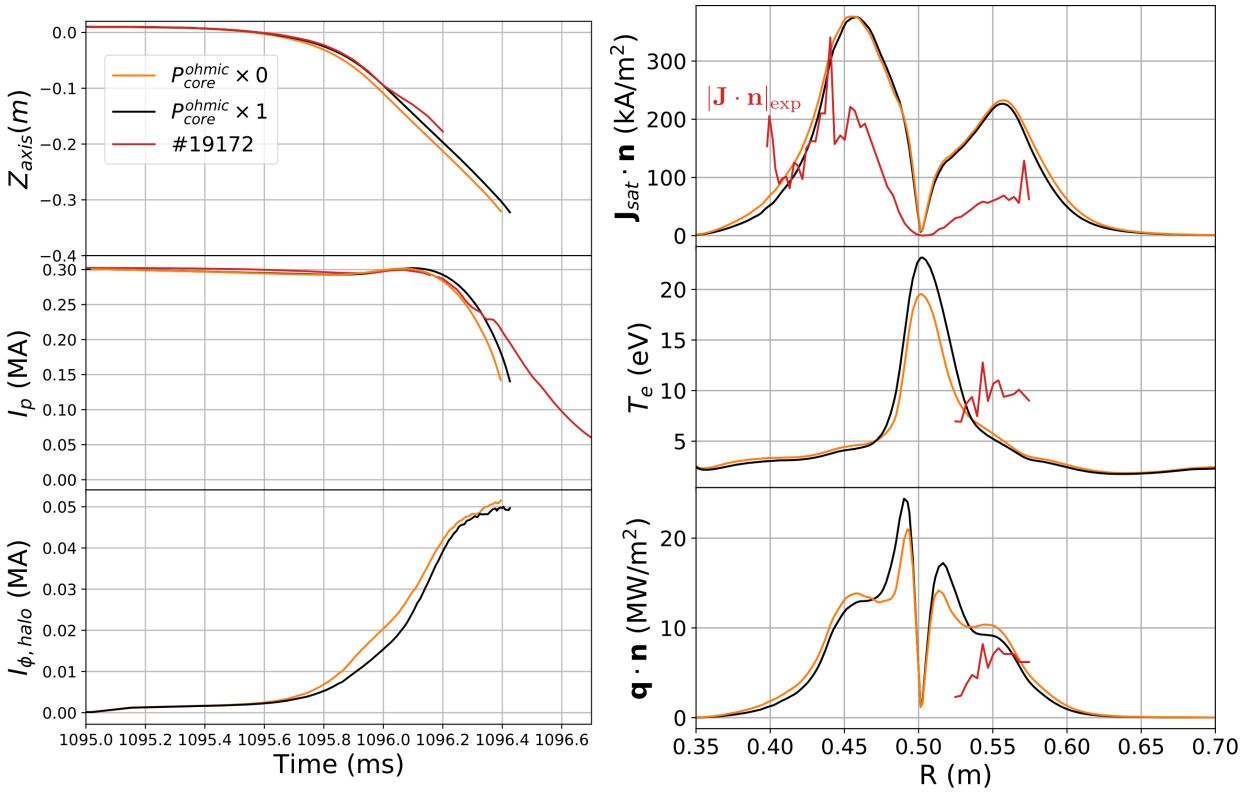

FIGURE 14: (Left) Vertical position of the magnetic axis, total toroidal plasma current and toroidal halo current in the plasma as function of time. (Right) Normal ion saturation current density, electron temperature and normal heat flux on the divertor at $I_p = 0.7I_{p0} = 0.21$ MA as function of the major radius. The black line corresponds to the base simulation and the yellow line to a case with the core Ohmic heating switched off. Note that in the upper right figure the absolute value of the experimental current density (red line) is plotted for reference.

6.1 Influence of resistivity and Ohmic heating

The plasma resistivity dictates the diffusion of the current density and influences the energy balance through Ohmic heating. In figure 12 we study the influence of the resistivity in the halo region by increasing it by a given factor only in that domain. Such an exercise can be viewed as a scan of the effective charge (Z_{eff}) in the halo region. In this case the resistivity is modified in both the induction equation ($\eta J_\parallel$ term) and in the pressure equation ($\eta J_\parallel^2$ term). The time traces in Figure 12 (left) indicate that increasing η_{halo} causes the vertical plasma motion and the current decay to take place earlier in time, although the decay rates do not change significantly. Also the toroidal halo current has a weak dependence on η_{halo}. The profiles at the time when $I_p = 0.7I_{p0}$ (Figure 12 right) show that the increase in η_{halo} flattens the J_{sat} profile as well as the temperature and heat flux profiles.

In order to distinguish between the effect of the resistive diffusion and the effect Ohmic heating, a set of cases were run where only the Ohmic heating term was multiplied by different factors in the halo region. These cases are presented in Figure 13, where it can be seen that the Ohmic heating alone can effectively increase T_e and q in the halo region. The increased Ohmic power acts as an additional heating source that is able to increase the plasma temperature and due to this also the pressure. For the factor range 1-6, the effect of the Ohmic power on the J_{sat} profile is very weak, which means that the halo pressure is due mostly through a temperature increase and thus at an almost constant particle flux (note that $J_{sat} \sim p/\sqrt{T}$). However when neglecting completely the Ohmic heating in the halo region (blue line), the J_{sat} magnitude is approximately reduced by a factor of 2. Note that in this case, the total toroidal halo current is not rigidly limited to J_{sat} in the $\pm$ 6 cm near the tangency point due to numerical reasons, as described before, and this allows a significant amount of halo current to flow in this region. To conclude, the effect of the Ohmic heating on the J_{sat} profile for $Z_{eff} \geq 1$ is very weak, but if the term is not included, the profile's amplitude can be reduced significantly. Finally this exercise proves that the profile flattening observed in figure 12 with increasing resistivity originates from current diffusion and not from Ohmic heating.

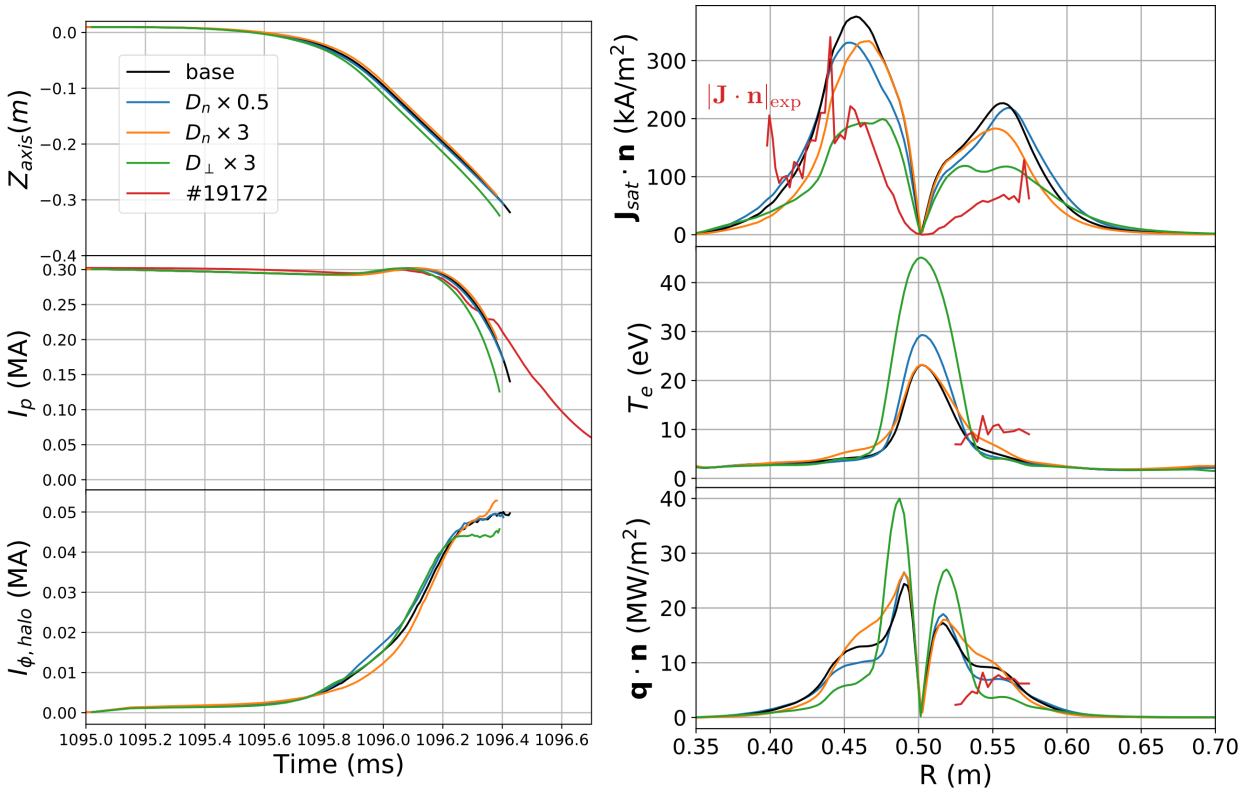

FIGURE 15: (Left) Vertical position of the magnetic axis, total toroidal plasma current and toroidal halo current in the plasma as function of time. (Right) Normal ion saturation current density, electron temperature and normal heat flux on the divertor at $I_p = 0.7 I_{p0} = 0.21$ MA as function of the major radius. The legends correspond to a case with D_n increased by a factor of 3 in all the plasma (green line), a case with D_n decreased by a factor of 2 (yellow line), a case with the ion diffusion increased by a factor of 3 (blue line), the base simulation (black line) and the experimental results (red line). Note that in the upper right figure the absolute value of the experimental current density (red line) is plotted for reference.

The effect of the heating power crossing the LCFS on the profiles along the divertor is studied in figure 14. We remind that in these simulations no auxiliary heating is employed, and all heating power comes from Ohmic heating. A case with the Ohmic heating turned off in the core (blue curve) shows that the core power has a small effect on the divertor profiles when compared to the standard case (black line) as it would be expected since the power flowing in the halo from the core is much smaller than the power directly deposited in the halo by Ohmic heating. For example for the Base simulation at $t = 1096.38$ ms (70% of I_{p0}), the power deposited by Ohmic heating in the core is 1.1 MW and the power directly deposited in the halo region by Ohmic heating is 7.8 MW.

6.2 Influence of particle and heat diffusion coefficients

The particle diffusion coefficients can directly affect the distribution of the plasma density and therefore can modify the ion saturation current density. In Figure 15 the standard simulation is repeated with different ion and neutral particle diffusion coefficients. When increasing the neutral particle diffusion coefficient by a factor of three (yellow line), the plasma density in the far SOL is reduced and the temperature increases, although the overall J_{sat} profile is not strongly modified. A larger D_n tends to decrease the plasma density at the wall due to the increase of the neutral mean free path (i.e. the ion particle source locally decreases as the neutrals are ionized at a further distance from the wall). Decreasing this coefficient by a factor of two shows a small effect in the J_{sat} profile, with a weak tendency to be increased in the far SOL. The increase of the ion diffusion coefficient by a factor of three (green line) has a larger effect on the J_{sat} profile. In this case the augmented D can diffuse the plasma density at the wall and decrease J_{sat} by about a factor of 2. Note that temperature does not increase accordingly and that finally the heat flux is reduced away from the contact point (e.g. at $R = 0.45$ m). The reason is that a smaller J_{sat} limiting the current flow away from the contact point, obliges the halo current to be re-induced near the LCFS and to deposit its associated Ohmic heating in that region instead.

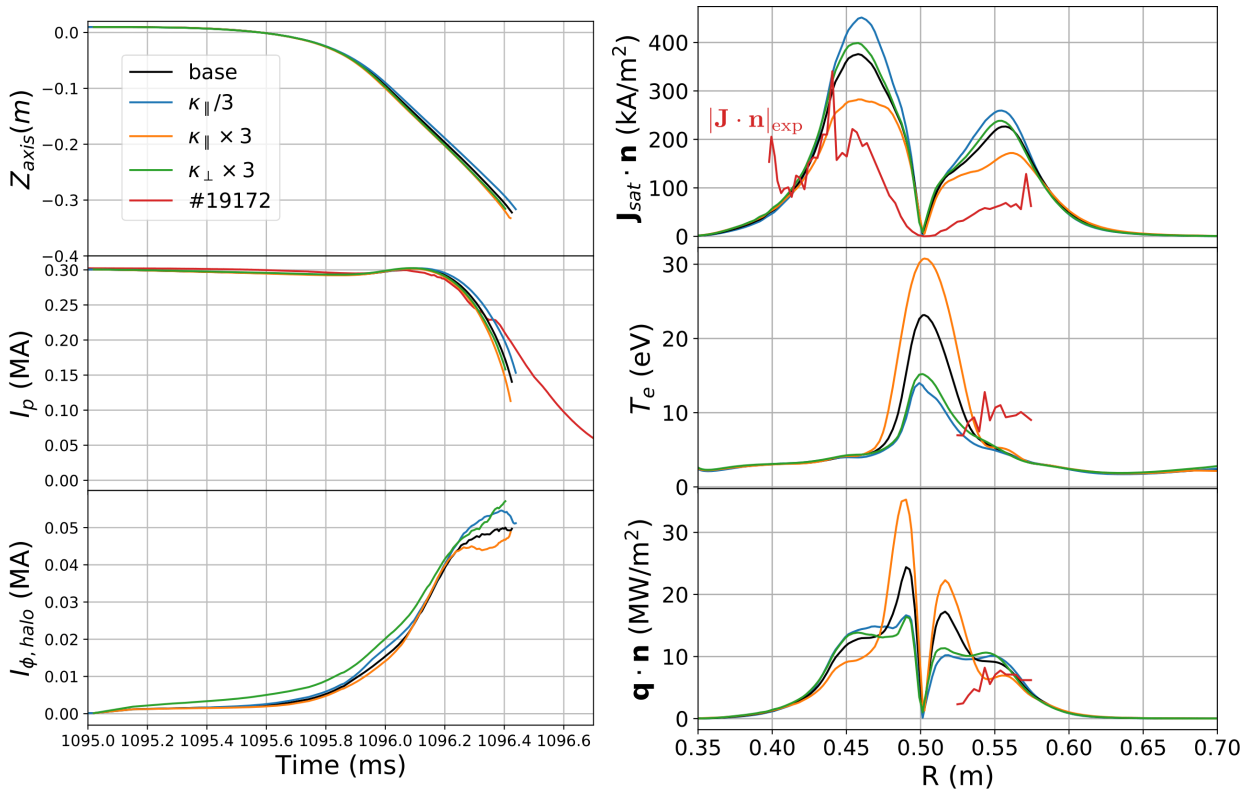

FIGURE 16: (Left) Vertical position of the magnetic axis, total toroidal plasma current and toroidal halo current in the plasma as function of time. (Right) Normal on saturation current density, electron temperature and parallel heat flux on the divertor at $I_p = 0.7I_{p0} = 0.21$ MA as function of the major radius. The legends correspond to cases with $\kappa_\parallel$ decreased and increased by a factor of 3 (yellow and green curves), a case with $\kappa_\perp$ increased by a factor of 3 (blue line) the base simulation (black line) and the experimental results (red line). Note that in the upper right figure the absolute value of the experimental current density (red line) is plotted for reference.

For steady state plasmas, the ratio between the perpendicular and the parallel heat conduction coefficients typically determines the width of the heat flux profile in the SOL. However for the considered VDE case, increasing the $\kappa_\perp/\kappa_\parallel$ ratio by a factor of three (either by modifying $\kappa_\perp$ or $\kappa_\parallel$) does not increase the width or the magnitude of the heat flux and the J_{sat} profiles (see blue and green lines of Figure 16). This indicates that during VDEs the SOL width is determined by other processes such as the resistive current diffusion shown in the previous section. However the increase of the parallel heat conduction by a factor of three (yellow line of Figure 16) is able to reduce the J_{sat} profile more significantly. In this case the divertor temperature near the limiter point raises as the upstream temperature is conducted faster along the field lines. As the LCFS region is hotter and therefore more electrically conducting, a significant fraction of the toroidal halo current is preferentially induced near the LCFS and deposits its associated Ohmic heating in that region, leading to the decrease of the J_{sat} magnitude at a further distance in the SOL (e.g. at $R = 0.45$ m).

7 Conclusions

In this paper a fully self-consistent model for halo currents has been presented and explored numerically with the JOREK code. The reduced MHD model includes an equation for neutral particles and a set of advanced boundary conditions. A boundary condition for the electrostatic potential (Φ) has been implemented in order to limit the halo current density (J) to the ion saturation current ($J_{sat} \sim n\sqrt{T}$) as expected from basic sheath plasma physics and observed in recent COMPASS experiments [1]. The boundary condition for Φ requires the implementation of sheath boundary conditions for the parallel velocity, the ion density, the neutral density and the temperature in order to obtain a self-consistent evolution of J_{sat} at the plasma-wall interface. The choice of realistic plasma parameters (e.g. Spitzer $\eta(T)$ and Spitzer-Härm $\kappa_\parallel(T)$) together with this model extends the status of halo current simulations beyond the present state of the art.

The limitation of the halo current density to J_{sat} is found to play a key role. The presented axisymmetric simulations of COMPASS VDE experiments show that with typical MHD boundary conditions ($\Phi = 0$), the current density becomes much larger than the ion saturation current leading to non-physical results. When the boundary condition for the electrostatic potential is applied during the VDE, the halo current density is always limited by the ion saturation current $J \approx J_{sat}$ as observed in experiments, implying that the halo current density is mainly given by the particle density. In this case both the halo width and total halo current are reduced in comparison to the case in which the current density is not limited. The implementation of such boundary condition requires a special treatment at the plasma-wall tangency point for numerical stability. In addition, the MHD simulations must be performed with a sufficiently low plasma viscosity in order to minimize current density gradients forming along the open field lines. The implementation of neutral particles is also found to be necessary when using sheath boundary conditions, otherwise the plasma-wall interface acts as a large ion sink that leads to very low particle densities and halo current densities.

Axisymmetric simulations of the COMPASS VDE discharge #19172 were compared with experimental measurements. Time traces of the vertical position and the plasma current show a good agreement with experiments at the beginning of the current quench ($t = 1096.0$ ms). A matching during the whole disruption is not expected as the axisymmetric modelling does not include yet important processes such as the thermal quench, impurity radiation and 3D MHD activity that can flatten the current density profile and affect the VDE dynamics. Our future work will be focused on 3D MHD simulations with the presented model to include these processes in a self-consistent form. Comparisons with the divertor probe measurements show that the position of the limiter point during the VDE is well captured by the simulations. The measured divertor profiles of the current density, the temperature and also the estimated heat flux were compared with the simulation results. The measured values are comparable in magnitude with the simulated values although significant discrepancies can be observed at certain radial locations (differences can be larger than a factor of two).

As the ion saturation current limit is found to determine the halo current density profile, the effect on the parameter choice on J_{sat} has been studied. In this respect the resistivity in the halo region flattens the J_{sat} profile through resistive diffusion, leading to an increased halo width. The dependencies of J_{sat} on the neutral particle diffusion and on the heat conduction coefficients are weaker than for the resistivity. However J_{sat} is also sensitive to the ion diffusion coefficient, which can reduce its magnitude considerably by reducing the plasma density at the boundary. In all

the performed parametric studies the total halo current is only weakly affected by the specific parameter choice whether it affects or not J_{sat}. This implies that the current flow limit by J_{sat} for the halo current density has a stronger impact on the halo width than on the total halo current with the latter being determined by VDE dynamics.

Although the regime $J_{\parallel} \approx J_{sat}$ is found in these COMPASS tokamak disruptions, it cannot be concluded that in all tokamak disruptive plasmas $J_{\parallel}$ will reach the J_{sat} limit (i.e. $J_{\parallel} < J_{sat}$ could be possible). $J_{\parallel}$ and J_{sat} are driven by different physics mechanisms: voltage during the disruptions for $J_{\parallel}$ and edge plasma conditions, particularly plasma density, for J_{sat}. Therefore, there can be disruptive plasma conditions in which the limit imposed by J_{sat} on $J_{\parallel}$ plays no role on the halo current flow since $J_{\parallel}$ does not approach this limit. Assuming the same J_{sat} limitation for halo currents during ITER VDEs, the ITER halo width will scale like $I_{p0}/(q_{95}\, J_{sat})$ since present experiments indicate that the total halo current scales with I_{p0}/q_{95} [16, 9]. Future simulations will be conducted with the presented model in order to determine whether $J_{\parallel} \approx J_{sat}$ and the latter scaling are to be expected in ITER disruptions or not.

Acknowledgements

This work was supported by the ITER Monaco Fellowship Program. ITER is the Nuclear Facility INB no. 174. This paper explores physics processes during the plasma operation of the tokamak when disruptions take place; nevertheless the nuclear operator is not constrained by the results presented here. The views and opinions expressed herein do not necessarily reflect those of the ITER Organization. The simulations presented here have been performed using the Marconi-Fusion supercomputer. This work has been carried out within the framework of the EUROfusion Consortium and has received funding from the Euratom research and training program 2014-2018 and 2019-2020 under grant agreement No 633053. The views and opinions expressed herein do not necessarily reflect those of the European Commission. The work was co-funded by MEYS projects number 8D15001 and LM2018117. This work has been carried out within the framework of the project COMPASS-U: Tokamak for cutting-edge fusion research (No. CZ.02.1.01/0.0/0.0/16_019/0000768) and co-funded from European structural and investment funds.

References

[1] J. Adamek, F. Artola, A. Loarte, J. Cavalier, R. Pitts, J. Havlicek, E. Matveeva, M. Hron, and R. Panek. Halo current density limitation during VDE-induced disruptions in the COMPASS tokamak. *to be submitted*, 2020.

[2] J. Adamek, J. Seidl, J. Horacek, M. Komm, T. Eich, R. Panek, J. Cavalier, A. Devitre, M. Peterka, P. Vondracek, J. Stöckel, D. Sestak, O. Grover, P. Bilkova, P. Böhm, J. Varju, A. Havranek, V. Weinzettl, J. Lovell, M. Dimitrova, K. Mitosinkova, R. Dejarnac, M. Hron, and and. Electron temperature and heat load measurements in the COMPASS divertor using the new system of probes. *Nuclear Fusion*, 57(11):116017, aug 2017. doi:10.1088/1741-4326/aa7e09.

[3] F. Artola Such. *Free-boundary simulations of MHD plasma instabilities in tokamaks*. Theses, Université Aix Marseille, Nov. 2018. URL: https://tel.archives-ouvertes.fr/tel-02012234.

[4] K. J. Bunkers and C. R. Sovinec. The influence of boundary and edge-plasma modeling in computations of axisymmetric vertical displacement. *Physics of Plasmas*, 27(11):112505, 2020. arXiv:https://doi.org/10.1063/5.0023604, doi:10.1063/5.0023604.

[5] G. Counsell, J.-W. Ahn, R. Cohen, A. Kirk, P. Helander, R. Martin, D. Ryutov, A. Tabasso, H. Wilson, Y. Yang, et al. Exhaust, ELM, and halo physics using the MAST tokamak. *Nuclear fusion*, 43(10):1197, 2003.

[6] O. Czarny and G. Huysmans. Bézier surfaces and finite elements for MHD simulations. *Journal of computational physics*, 227(16):7423–7445, 2008. doi:10.1016/j.jcp.2008.04.001.

[7] E. Franck, M. Hölzl, A. Lessig, and E. Sonnendrücker. Energy conservation and numerical stability for the reduced mhd models of the non-linear jorek code. *arXiv preprint arXiv:1408.2099*, 2014.

[8] A. H. Glasser, C. R. Sovinec, R. A. Nebel, T. A. Gianakon, S. J. Plimpton, M. S. Chu, D. D. Schnack, and the NIMROD Team. The NIMROD code: a new approach to numerical plasma physics. *Plasma Physics and Controlled Fusion*, 41(3A):A747–A755, jan 1999. doi:10.1088/0741-3335/41/3a/067.

[9] R. Granetz, I. Hutchinson, J. Sorci, J. Irby, B. LaBombard, and D. Gwinn. Disruptions and halo currents in Alcator C-Mod. *Nuclear fusion*, 36(5):545, 1996. doi:10.1088/0029-5515/36/5/i02.

[10] T. Hender, J. Wesley, J. Bialek, A. Bondeson, A. Boozer, R. Buttery, A. Garofalo, T. Goodman, R. Granetz, Y. Gribov, O. Gruber, M. Gryaznevich, G. Giruzzi, S. Günter, N. Hayashi, P. Helander, C. Hegna, D. Howell, D. Humphreys, G. Huysmans, A. Hyatt, A. Isayama, S. Jardin, Y. Kawano, A. Kellman, C. Kessel, H. Koslowski, R. L. Haye, E. Lazzaro, Y. Liu, V. Lukash, J. Manickam, S. Medvedev, V. Mertens, S. Mirnov, Y. Nakamura, G. Navratil, M. Okabayashi, T. Ozeki, R. Paccagnella, G. Pautasso, F. Porcelli, V. Pustovitov, V. Riccardo, M. Sato, O. Sauter, M. Schaffer, M. Shimada, P. Sonato, E. Strait, M. Sugihara, M. Takechi, A. Turnbull, E. Westerhof, D. Whyte, R. Yoshino, H. Zohm, D. the ITPA MHD, and M. Group. Chapter 3: MHD stability, operational limits and disruptions. *Nuclear Fusion*, 47(6):S128–S202, jun 2007. doi:10.1088/0029-5515/47/6/s03.

[11] M. Hoelzl, G. Huijsmans, S. Pamela, M. Becoulet, E. Nardon, F. Artola, and B. N. et al. The JOREK non-linear extended MHD code and applications to large-scale instabilities and their control in magnetically confined fusion plasmas. *Nuclear Fusion (submitted)*, 2020. URL: https://arxiv.org/abs/2011.09120.

[12] M. Hölzl, P. Merkel, G. Huysmans, E. Nardon, E. Strumberger, R. McAdams, I. Chapman, S. Günter, and K. Lackner. Coupling JOREK and STARWALL codes for non-linear resistive-wall simulations. In *Journal of Physics: Conference Series*, volume 401, page 012010. IOP Publishing, 2012. doi:10.1088/1742-6596/401/1/012010.

[13] J. Horacek, J. Adamek, M. Komm, J. Seidl, P. Vondracek, A. Jardin, C. Guillemaut, S. Elmore, A. Thornton, and K. J. et al. Scaling of L-mode heat flux for ITER and COMPASS-U divertors, based on five tokamaks. *Nuclear Fusion*, 60(6):066016, 2020. doi:10.1088/1741-4326/ab7e47.

[14] D. A. Humphreys and A. G. Kellman. Analytic modeling of axisymmetric disruption halo currents. *Physics of Plasmas*, 6(7):2742–2756, 1999. doi:10.1063/1.873231.

[15] G. Huysmans and O. Czarny. MHD stability in X-point geometry: simulation of ELMs. *Nuclear fusion*, 47(7):659, 2007. doi:10.1088/0029-5515/47/7/016.

[16] P. Knight, G. Castle, A. Morris, A. Caloutsis, and C. Gimblett. Analysis of vertical displacement events and halo currents in COMPASS-D. *Nuclear Fusion*, 40(3):325–337, mar 2000. URL: https://doi.org/10.1088%2F0029-5515%2F40%2F3%2F304, doi:10.1088/0029-5515/40/3/304.

[17] I. Krebs, F. Artola, C. Sovinec, S. Jardin, K. Bunkers, M. Hoelzl, and N. Ferraro. Axisymmetric simulations of vertical displacement events in tokamaks: A benchmark of M3D-C1, NIMROD, and JOREK. *Physics of Plasmas*, 27(2):022505, 2020. doi:10.1063/1.5127664.

[18] L. Lao, H. S. John, R. Stambaugh, A. Kellman, and W. Pfeiffer. Reconstruction of current profile parameters and plasma shapes in tokamaks. *Nuclear fusion*, 25(11):1611, 1985. doi:10.1088/0029-5515/25/11/007.

[19] M. Lehnen, K. Aleynikova, P. Aleynikov, D. Campbell, P. Drewelow, N. Eidietis, Y. Gasparyan, R. Granetz, Y. Gribov, N. Hartmann, et al. Disruptions in ITER and strategies for their control and mitigation. *Journal of Nuclear Materials*, 463:39–48, 2015. doi:10.1016/j.jnucmat.2014.10.075.

[20] G. Matthews, S. Fielding, G. McCracken, C. Pitcher, P. Stangeby, and M. Ulrickson. Investigation of the fluxes to a surface at grazing angles of incidence in the tokamak boundary. *Plasma Physics and Controlled Fusion*, 32(14):1301, 1990. doi:10.1088/0741-3335/32/14/004.

[21] P. Merkel and E. Strumberger. Linear MHD stability studies with the STARWALL code. *arXiv preprint*, 2015. URL: https://arxiv.org/abs/1508.04911.

[22] S. Smith, S. Pamela, A. Fil, M. Hölzl, G. Huijsmans, A. Kirk, D. Moulton, O. Myatra, A. Thornton, and H. W. and. Simulations of edge localised mode instabilities in MAST-u super-x tokamak plasmas. *Nuclear Fusion*, 60(6):066021, may 2020. doi:10.1088/1741-4326/ab826a.

[23] P. C. Stangeby. The Bohm–Chodura plasma sheath criterion. *Physics of Plasmas*, 2(3):702–706, 1995. doi:10.1063/1.871483.

[24] P. C. Stangeby et al. *The plasma boundary of magnetic fusion devices*, volume 224. Institute of Physics Pub. Philadelphia, Pennsylvania, 2000.